

Initial Entropy and Electron Fraction

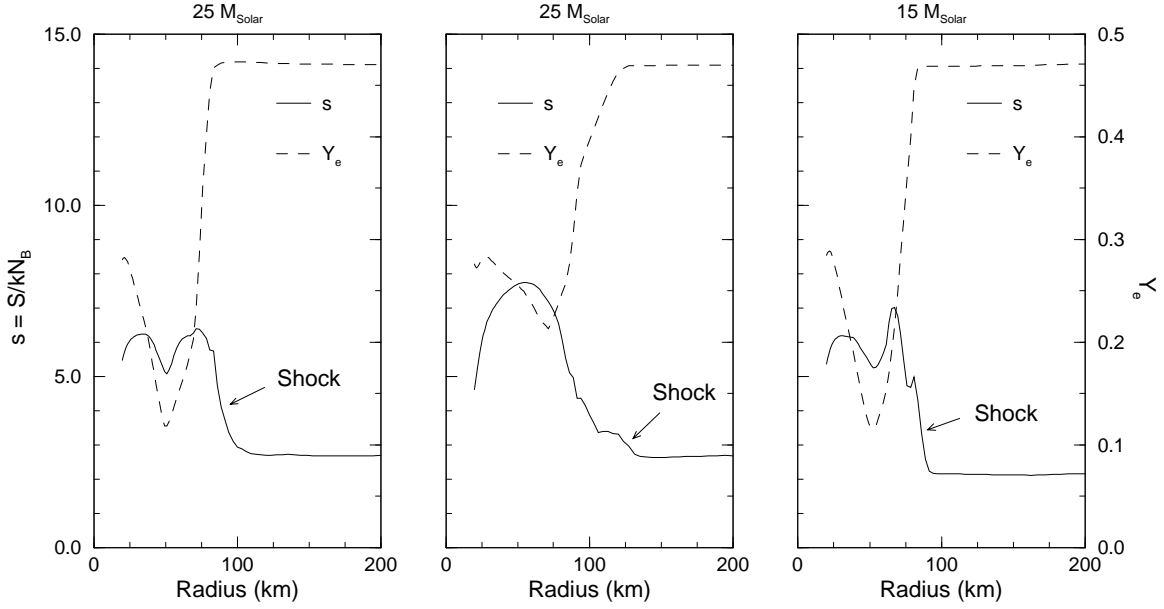


Fig. 1.— Initial entropy and electron fraction profiles of the $25 M_{\odot}$, $25 M_{\odot}$ “low-test”, and $15 M_{\odot}$ simulations.

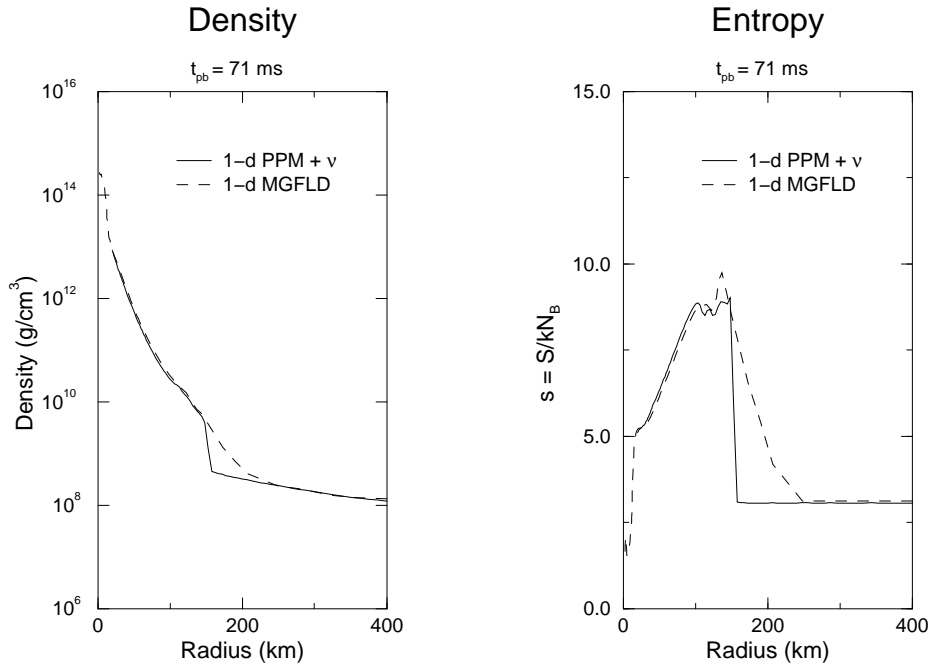


Fig. 2a.— Plot of density and entropy versus radius, comparing a simulation with one-dimensional PPM hydrodynamics and MGFLD neutrino transport (simulation B) to a simulation with one-dimensional Lagrangian hydrodynamics and MGFLD neutrino transport. The comparison is made 62 ms into the run.

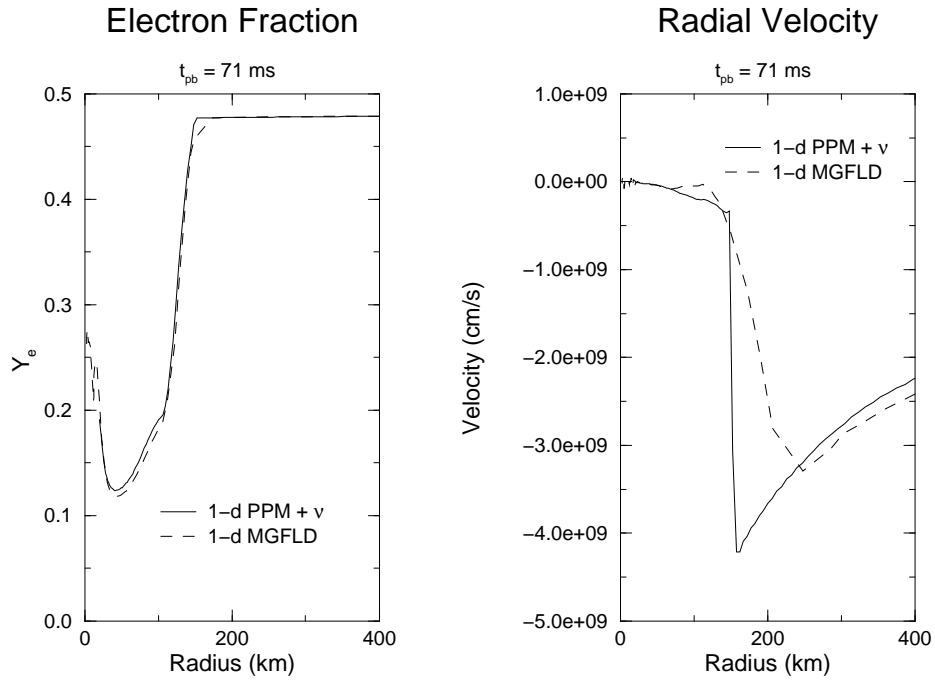


Fig. 2b.— Plot of electron fraction and radial velocity vs. radius for the same comparison shown in Figure 2a.

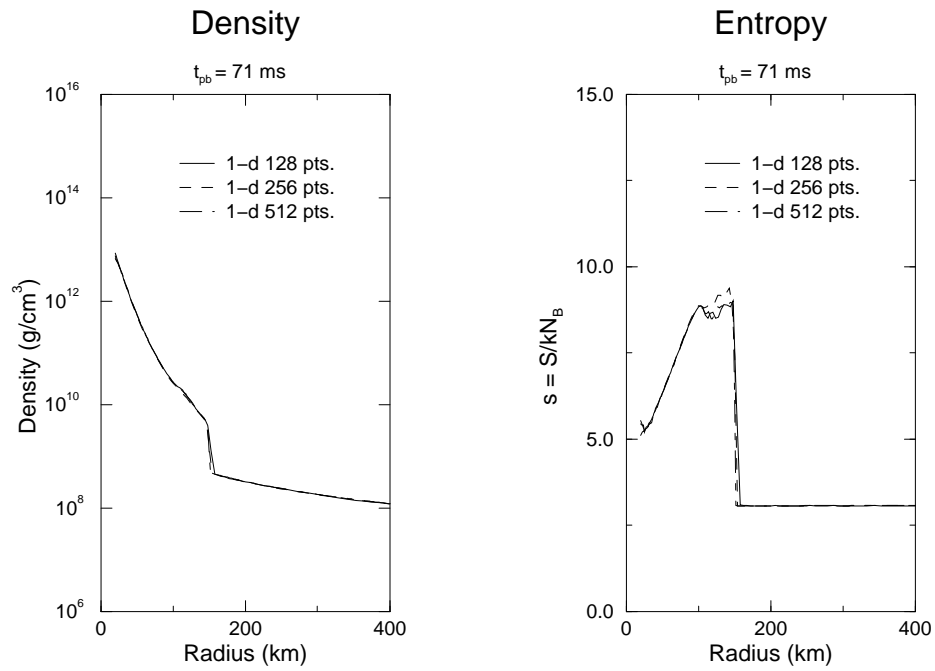


Fig. 2c.— Plots of the density and entropy profiles at $t_{pb} = 71$ ms, for three different radial grid resolutions in our one-dimensional PPM simulations.

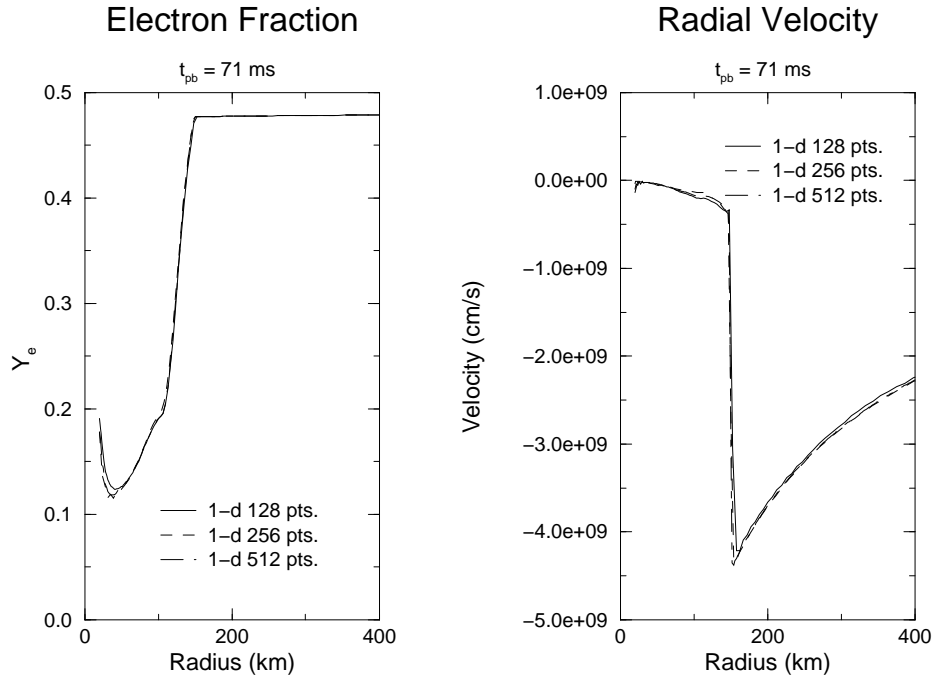


Fig. 2d.— Plots of the electron fraction and radial velocity profiles at $t_{pb} = 71$ ms, for three different radial grid resolutions in our one-dimensional PPM simulations.

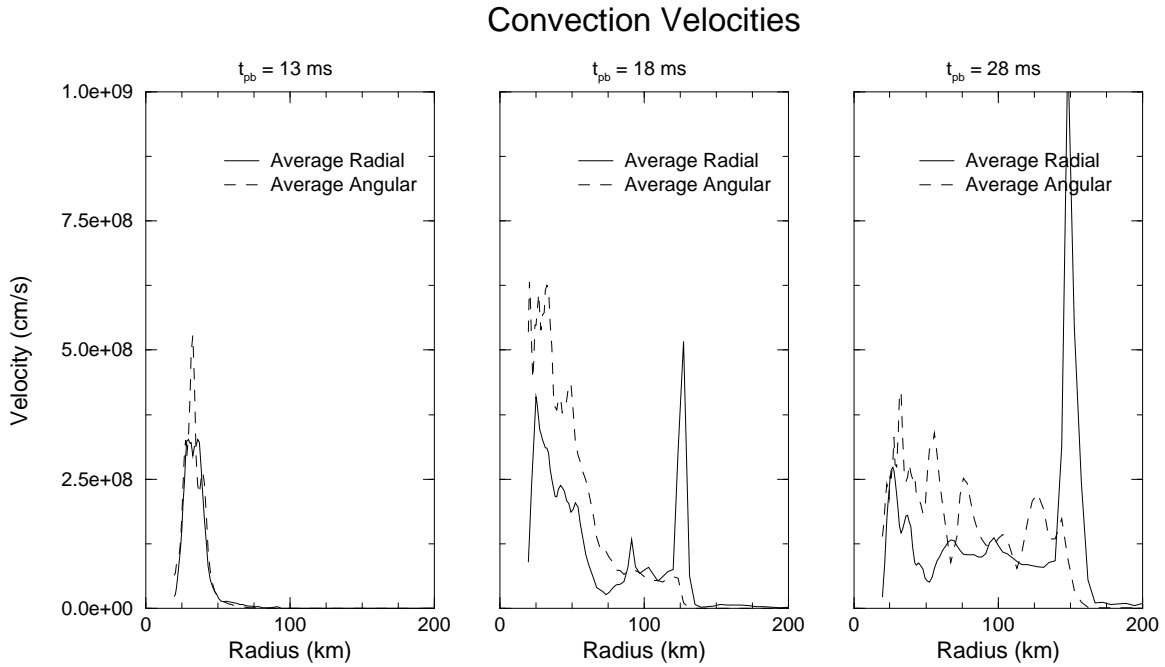


Fig. 3b.— Plots of the angle-averaged radial and angular convection velocities corresponding to the three entropy snapshots in Figure 3a.

Angle Averaged Entropy and Electron Fraction

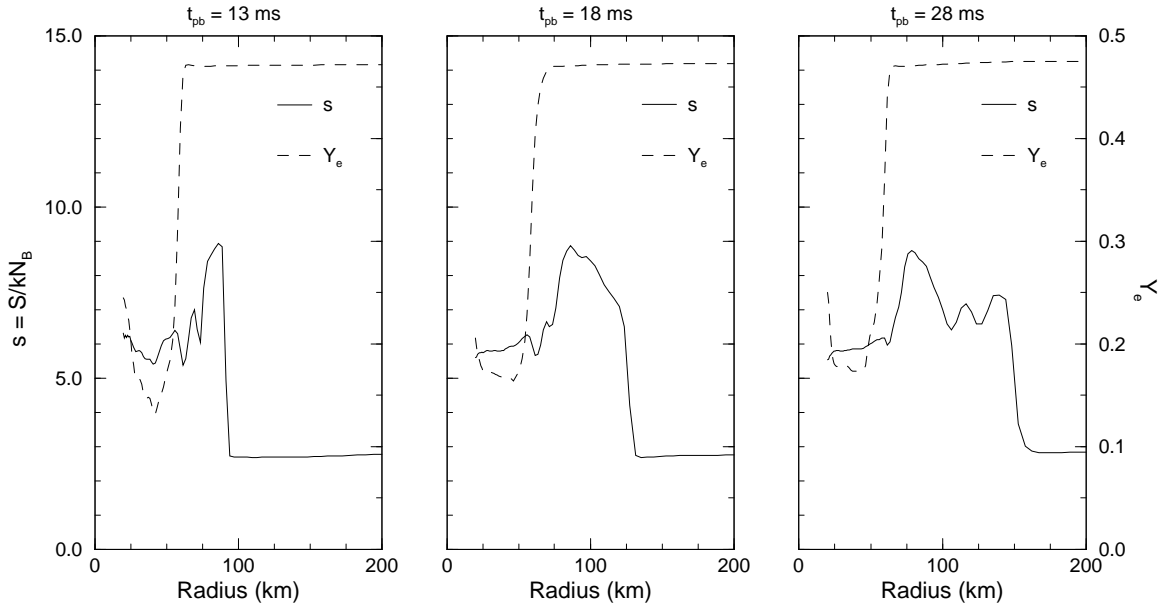


Fig. 3c.— Plots showing the angle-averaged entropy and electron fraction corresponding to the three entropy snapshots in Figure 3a.

Convection Velocities

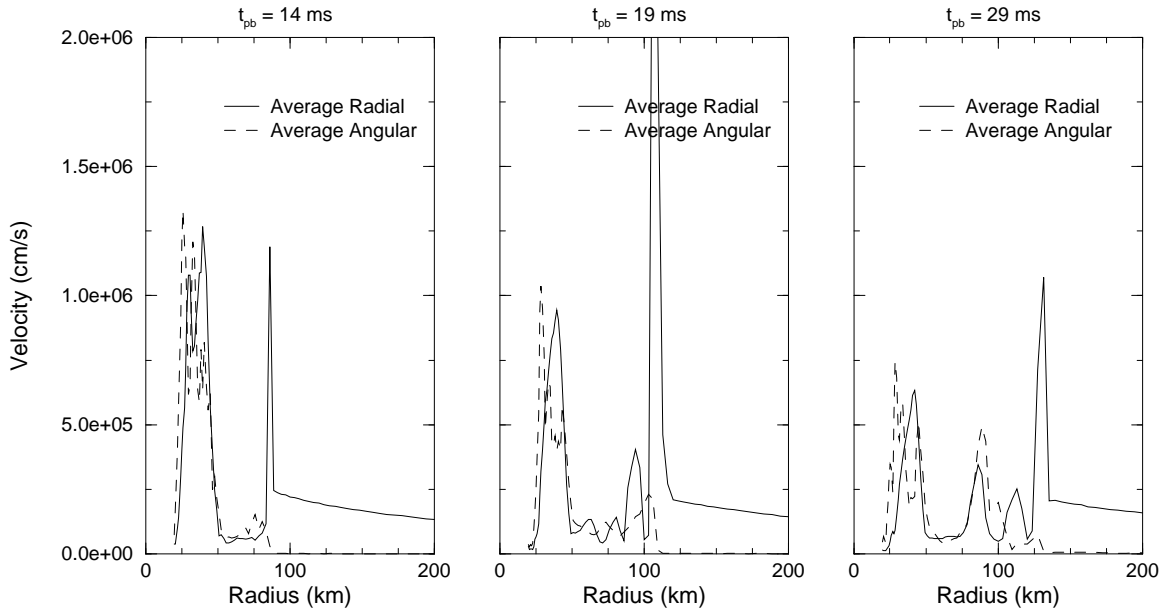


Fig. 4b.— Plots of the angle-averaged radial and angular convection velocities corresponding to the three entropy snapshots in Figure 4a.

Angle Averaged Entropy and Electron Fraction

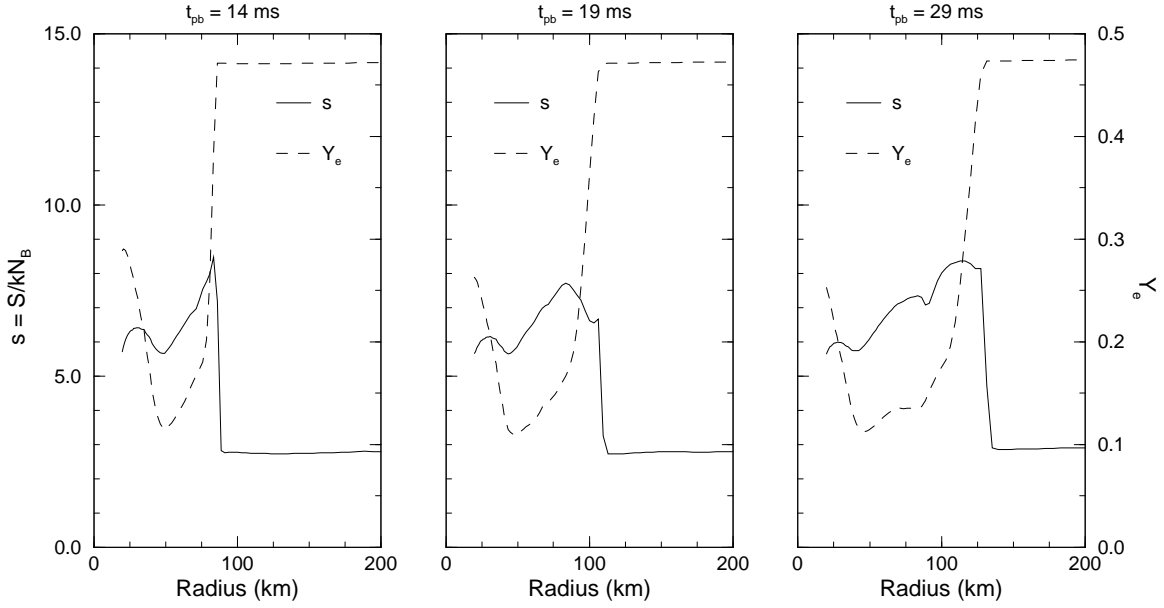


Fig. 4c.— Plots showing the angle-averaged entropy and electron fraction corresponding to the three entropy snapshots in Figure 4a.

Angle Averaged Radial Velocities

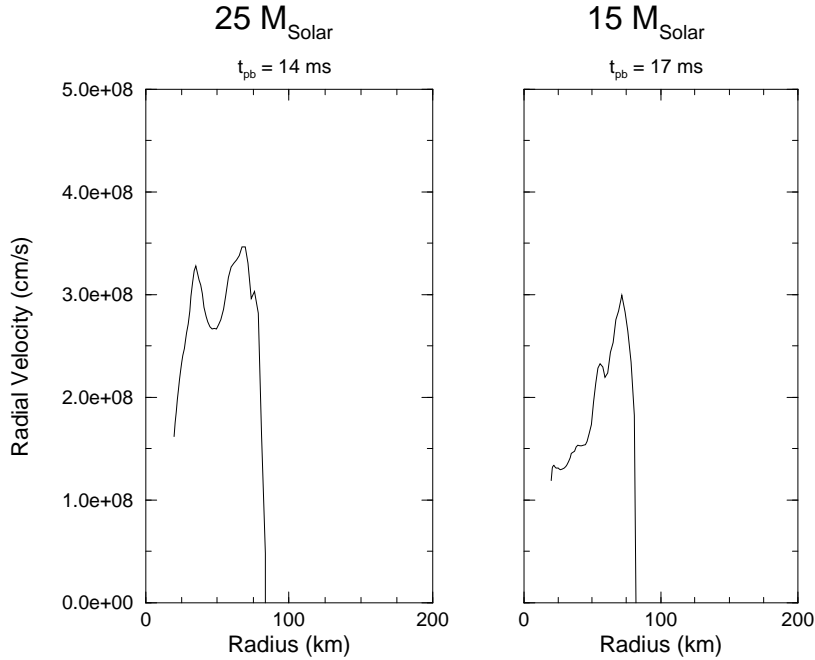


Fig. 4d.— Plot of the angle-averaged radial velocities in the innermost region of the two-dimensional grid for our “fiducial” 25 M_⊙ and 15 M_⊙ simulations (D and L).

Convection Velocities

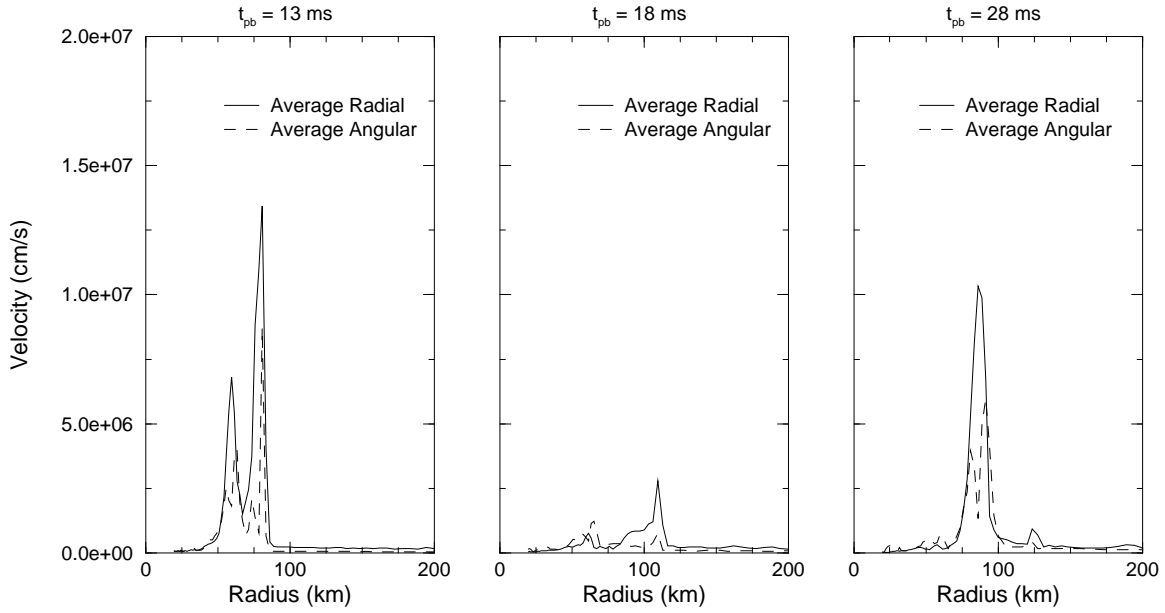


Fig. 5b.— Plots of the angle-averaged radial and angular convection velocities corresponding to the three entropy snapshots in Figure 5a.

Angle Averaged Entropy and Electron Fraction

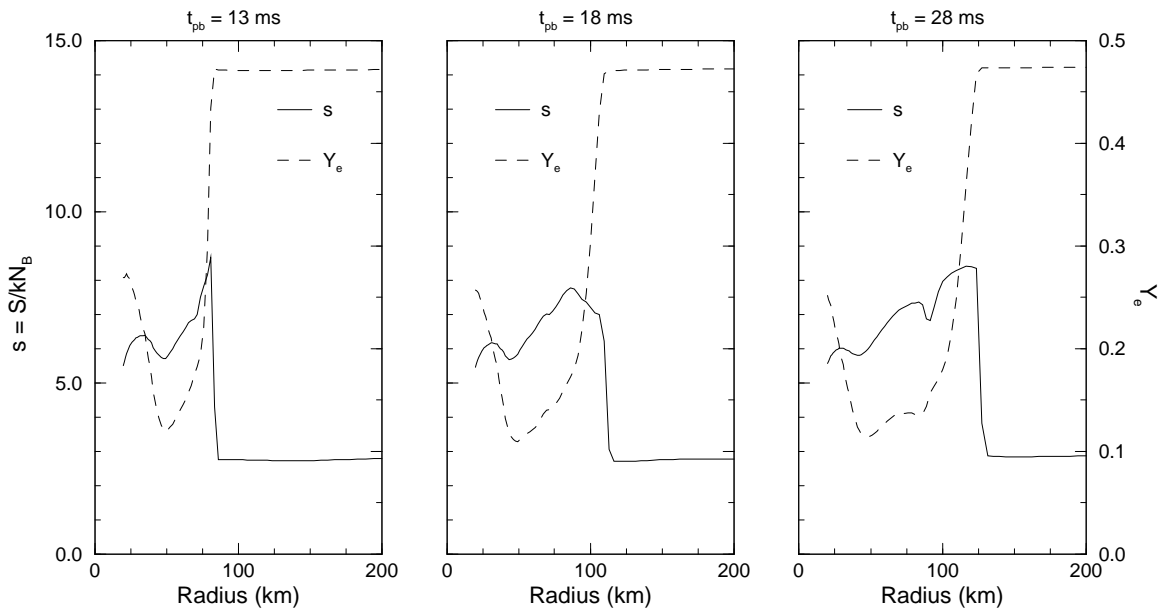


Fig. 5c.— Plots showing the angle-averaged entropy and electron fraction corresponding to the three entropy snapshots in Figure 5a.

Convection Velocities

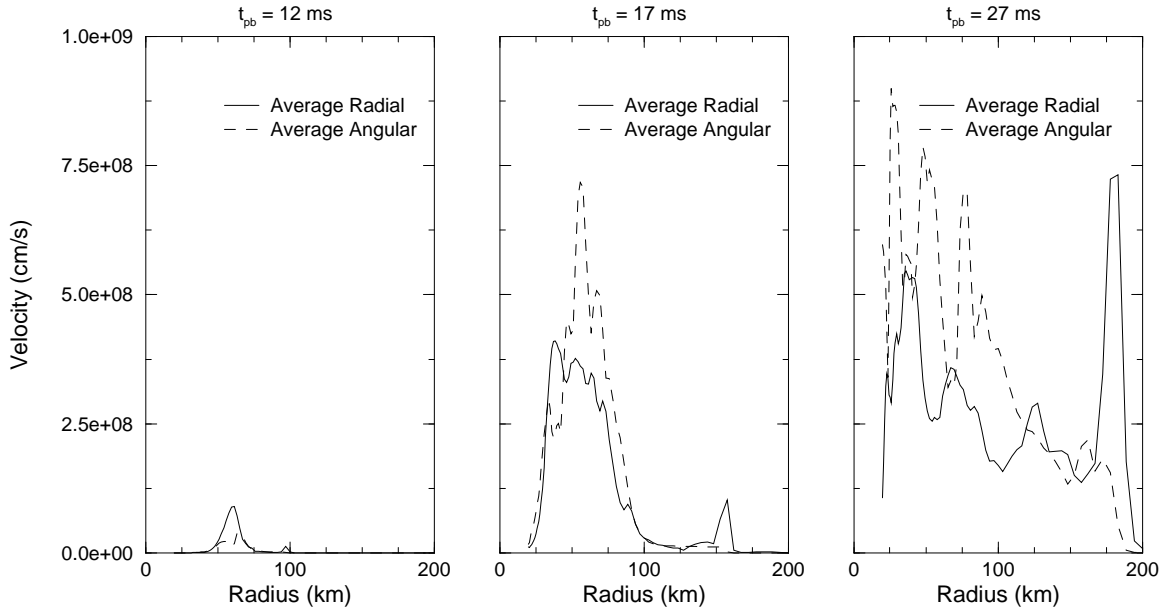


Fig. 6b.— Plots of the angle-averaged radial and angular convection velocities corresponding to the three entropy snapshots in Figure 6a.

Angle Averaged Entropy and Electron Fraction

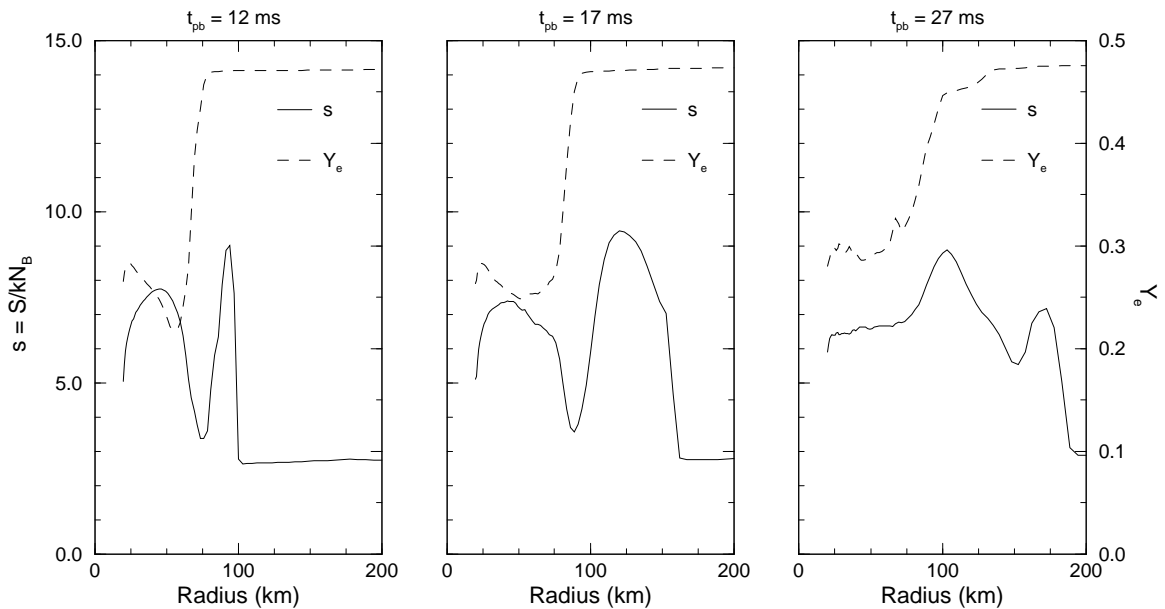


Fig. 6c.— Plots showing the angle-averaged entropy and electron fraction corresponding to the three entropy snapshots in Figure 6a.

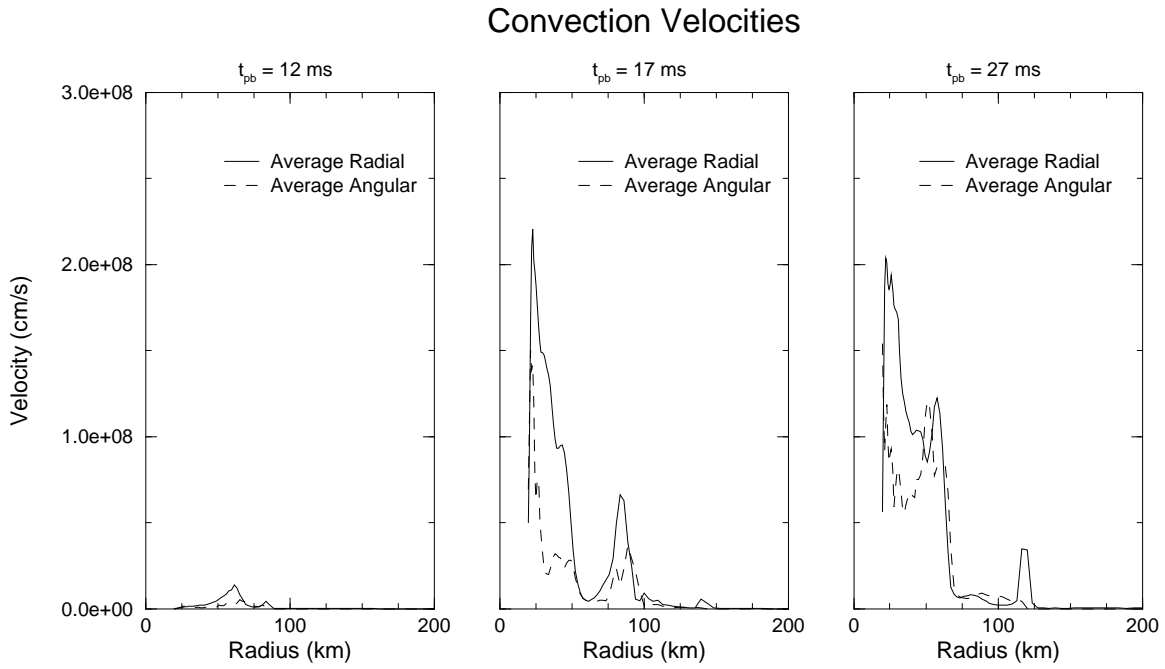


Fig. 7b.— Plots of the angle-averaged radial and angular convection velocities corresponding to the three entropy snapshots in Figure 7a.

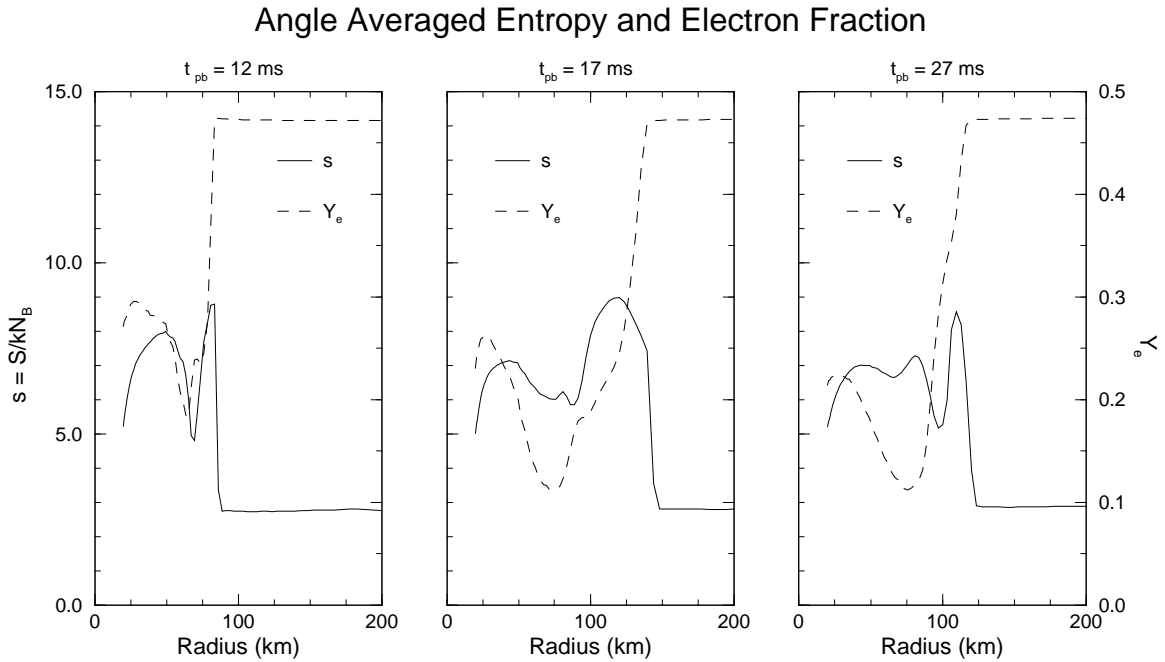


Fig. 7c.— Plots showing the angle-averaged entropy and electron fraction corresponding to the three entropy snapshots in Figure 7a.

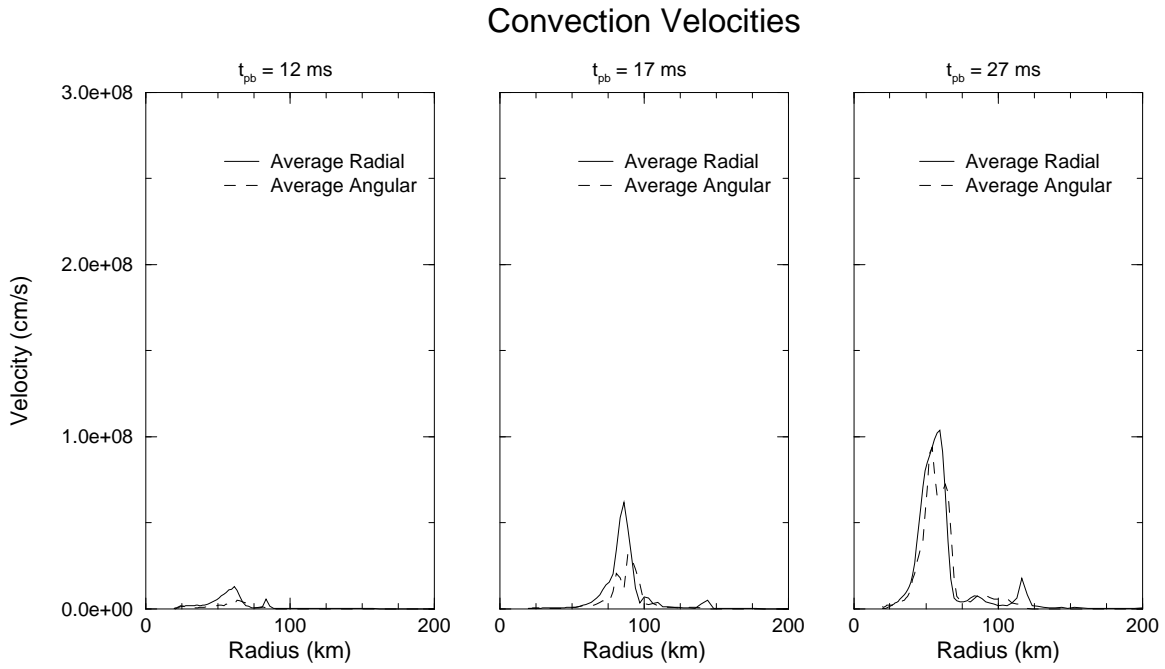


Fig. 8b.— Plots of the angle-averaged radial and angular convection velocities corresponding to the three entropy snapshots in Figure 8a.

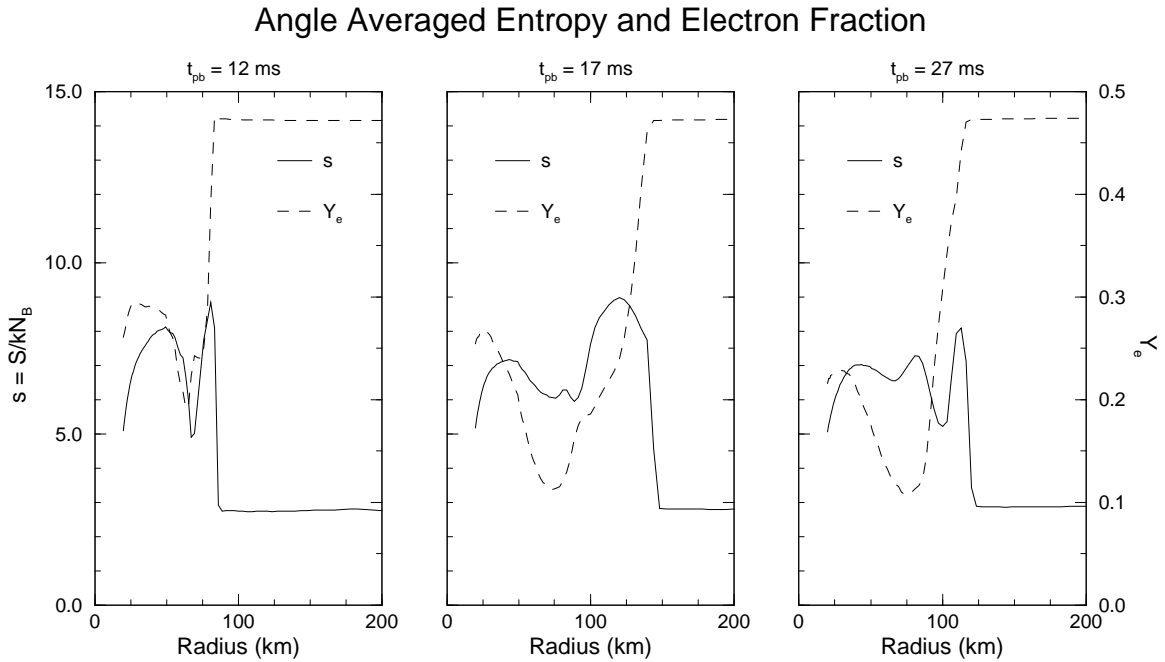


Fig. 8c.— Plots showing the angle-averaged entropy and electron fraction corresponding to the three entropy snapshots in Figure 8a.

Convection Velocities

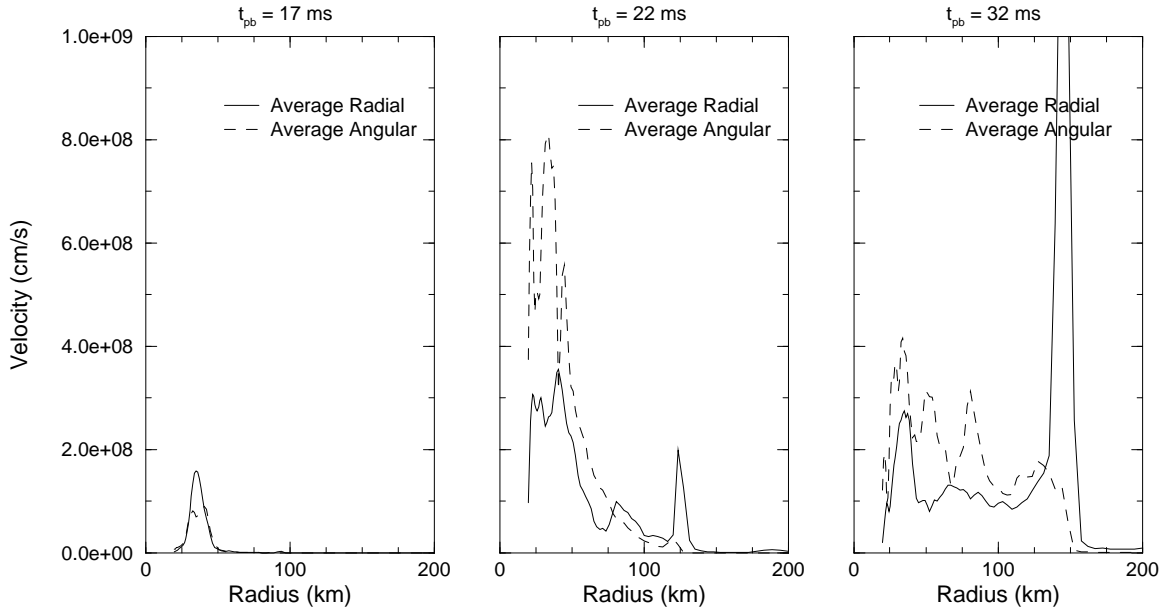


Fig. 10b.— Plots of the angle-averaged radial and angular convection velocities corresponding to the three entropy snapshots in Figure 10a.

Angle Averaged Entropy and Electron Fraction

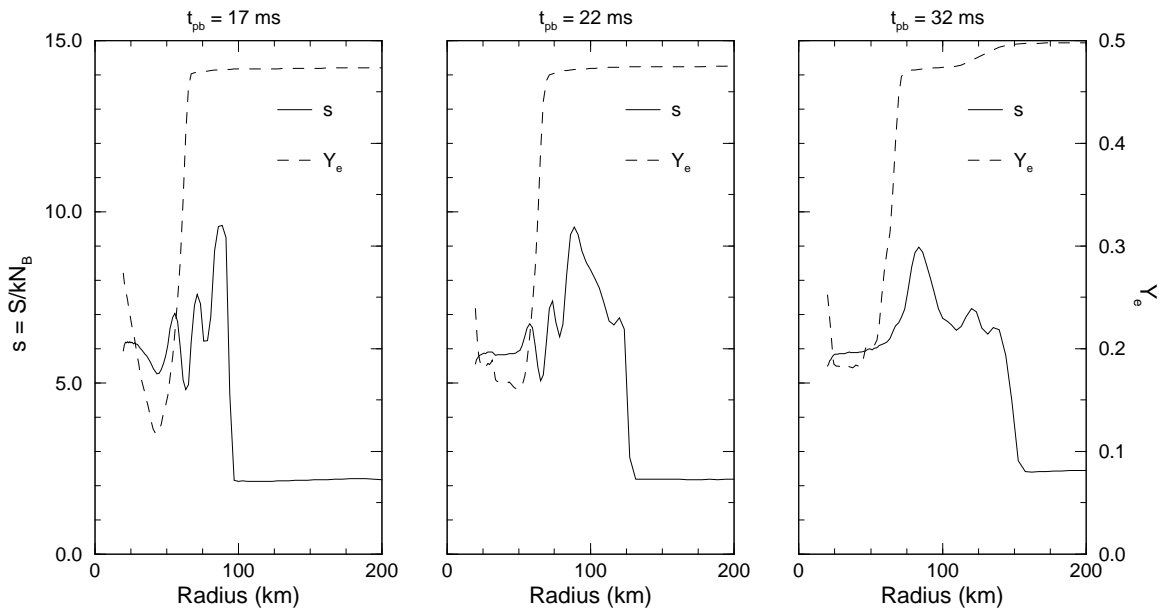


Fig. 10c.— Plots showing the angle-averaged entropy and electron fraction corresponding to the three entropy snapshots in Figure 10a.

Convection Velocities

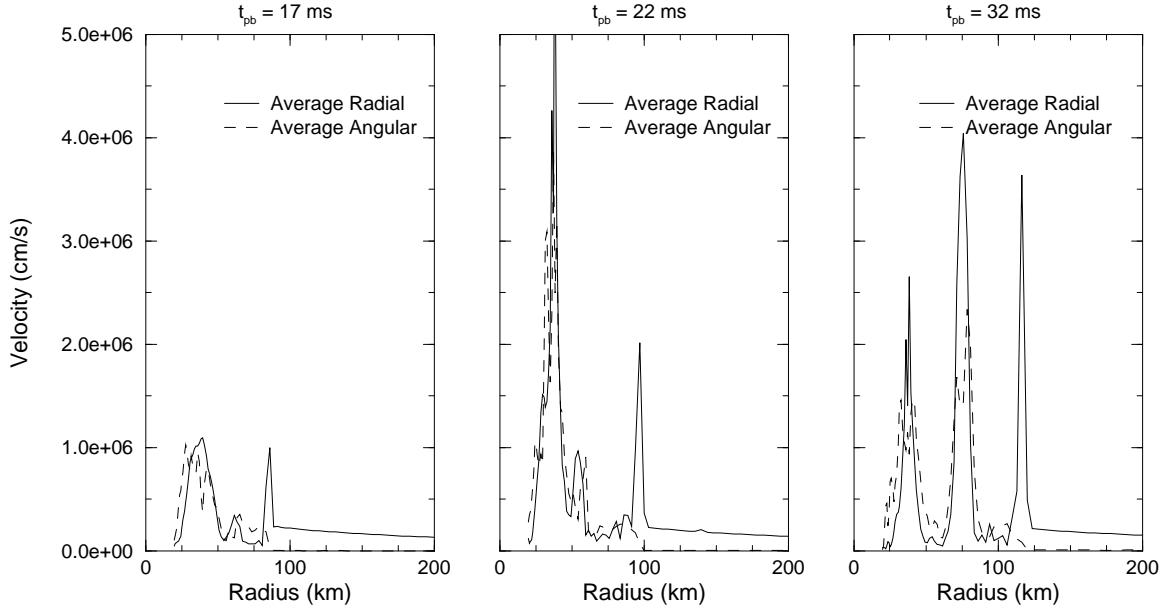


Fig. 11b.— Plots of the angle-averaged radial and angular convection velocities corresponding to the three entropy snapshots in Figure 11a.

Angle Averaged Entropy and Electron Fraction

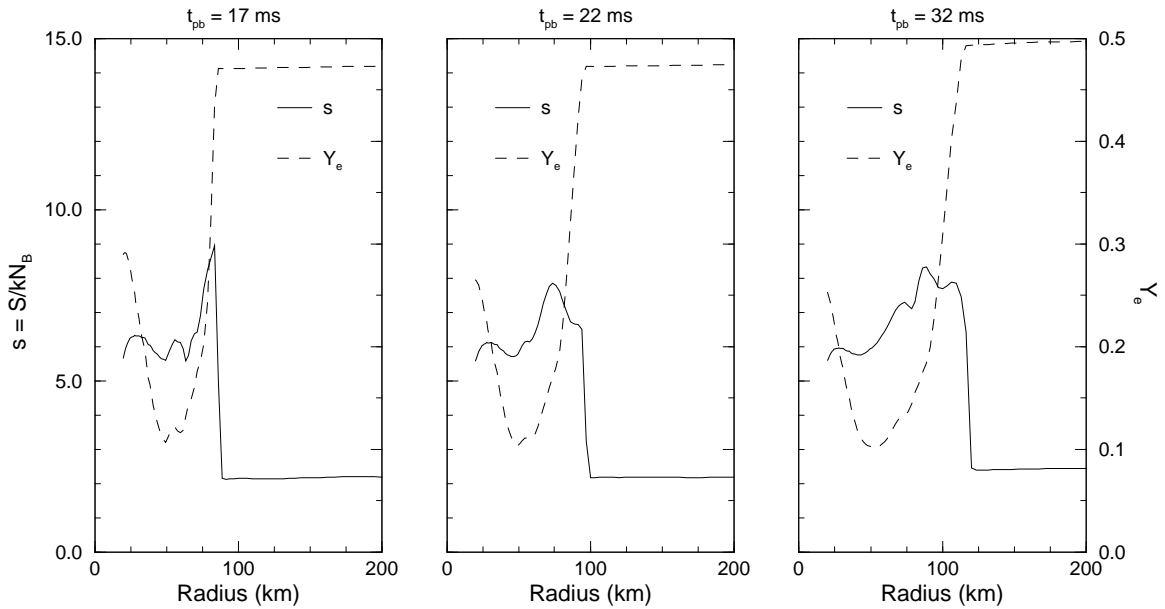


Fig. 11c.— Plots showing the angle-averaged entropy and electron fraction corresponding to the three entropy snapshots in Figure 11a.

Convection and Equilibration Time Scales

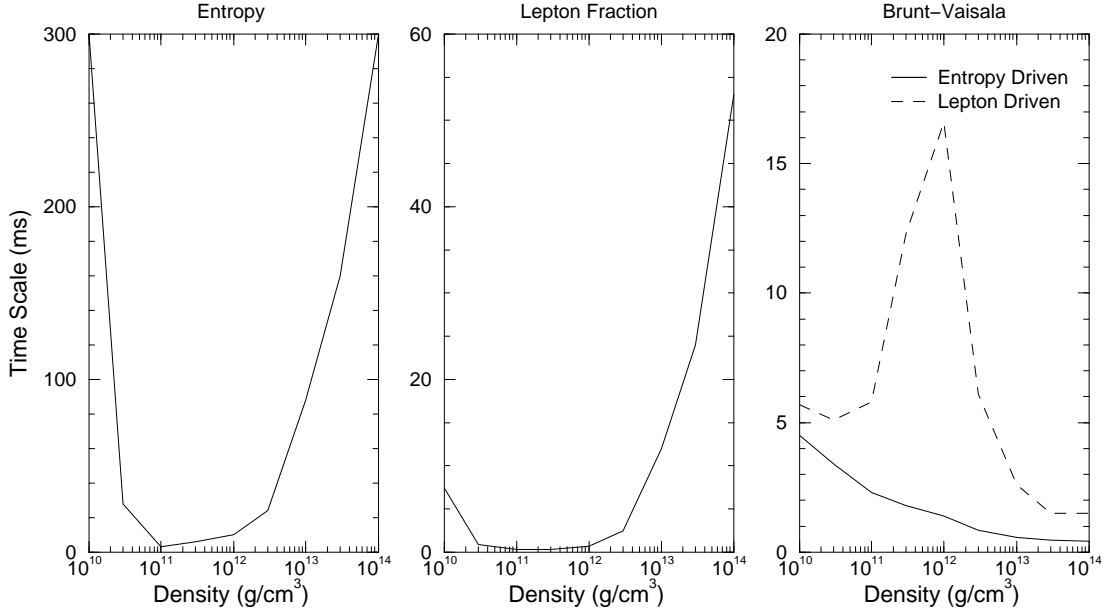


Fig. 12.— Plots showing the entropy and lepton-fraction equilibration time scales, and the convection (Brunt-Väisälä) time scales, as a function of density.

ENTROPY

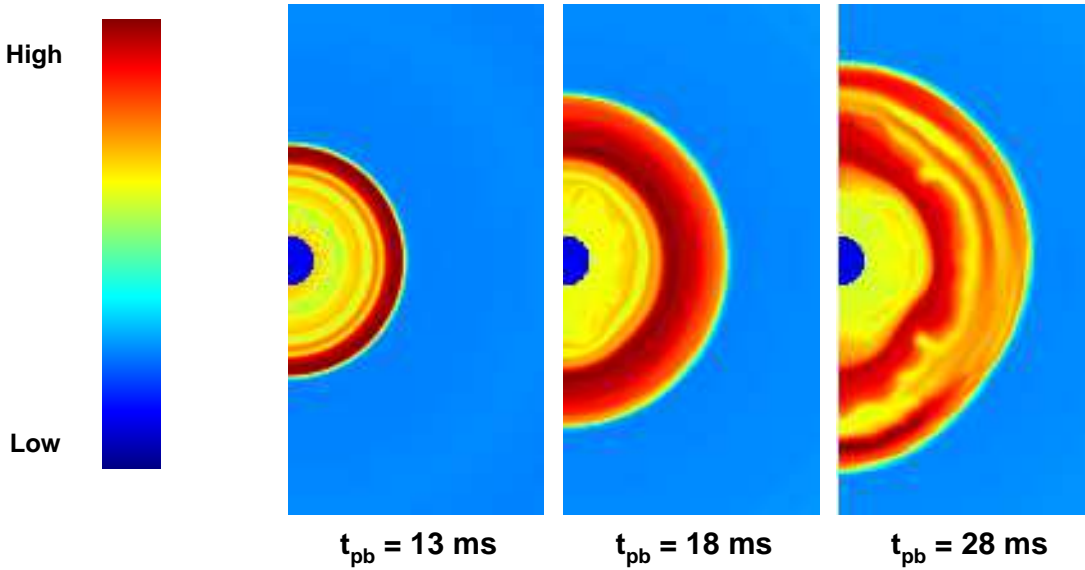


Fig. 3a.— (simulation C). The two-dimensional plots showing the entropy evolution of the $25 M_{\odot}$ model in a simulation without neutrino transport (simulation C).

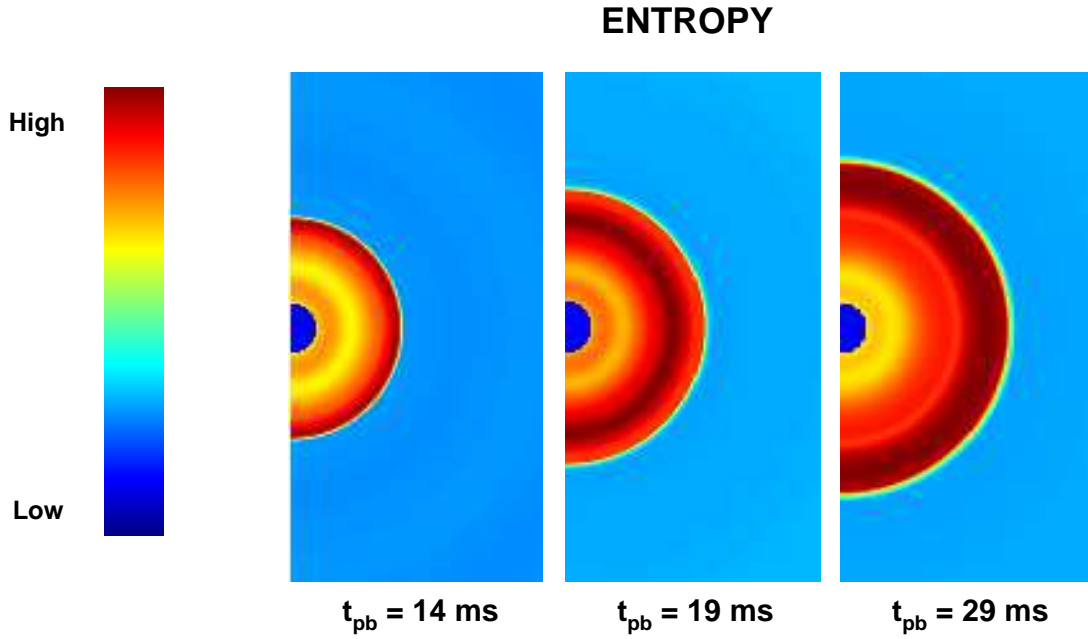


Fig. 4a.— Two-dimensional plots showing the entropy evolution of the $25 M_{\odot}$ model in a simulation with neutrino transport (simulation D).

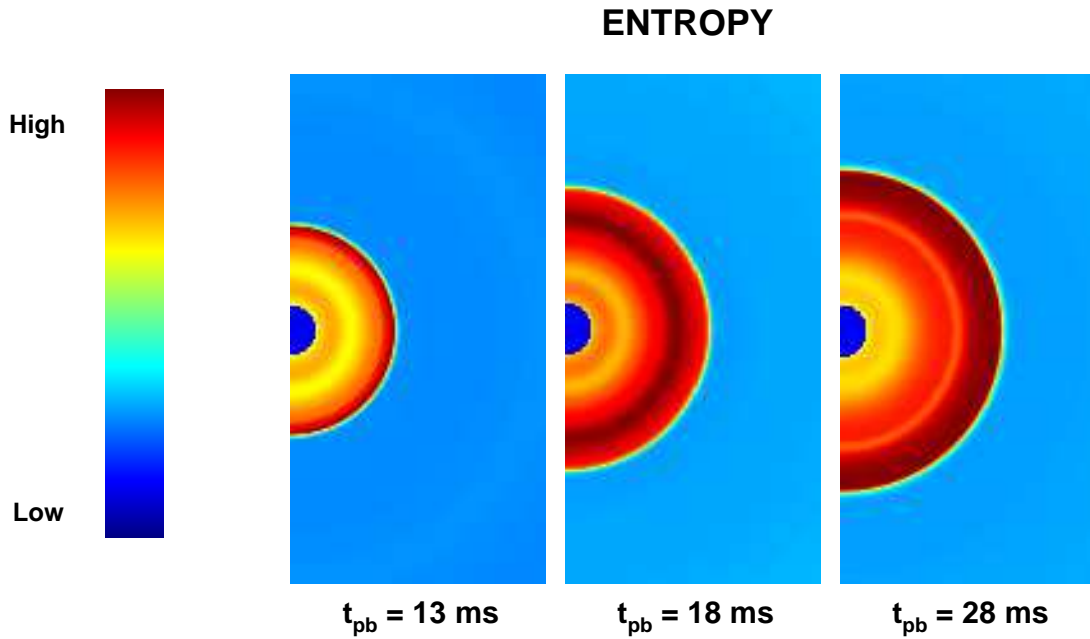


Fig. 5a.— Two-dimensional plots showing the entropy evolution of the $25 M_{\odot}$ model in a simulation with neutrino transport that includes “finite-time” effects (simulation E).

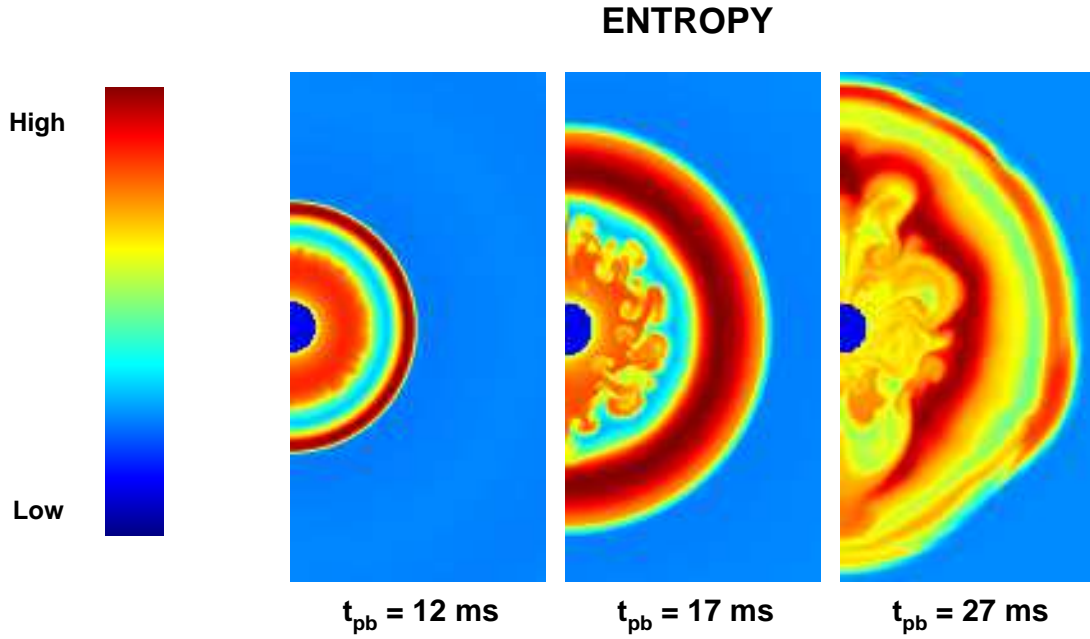


Fig. 6a.— Two-dimensional plots showing the entropy evolution of the $25 M_{\odot}$ model in a “low-test” simulation without neutrino transport (simulation F).

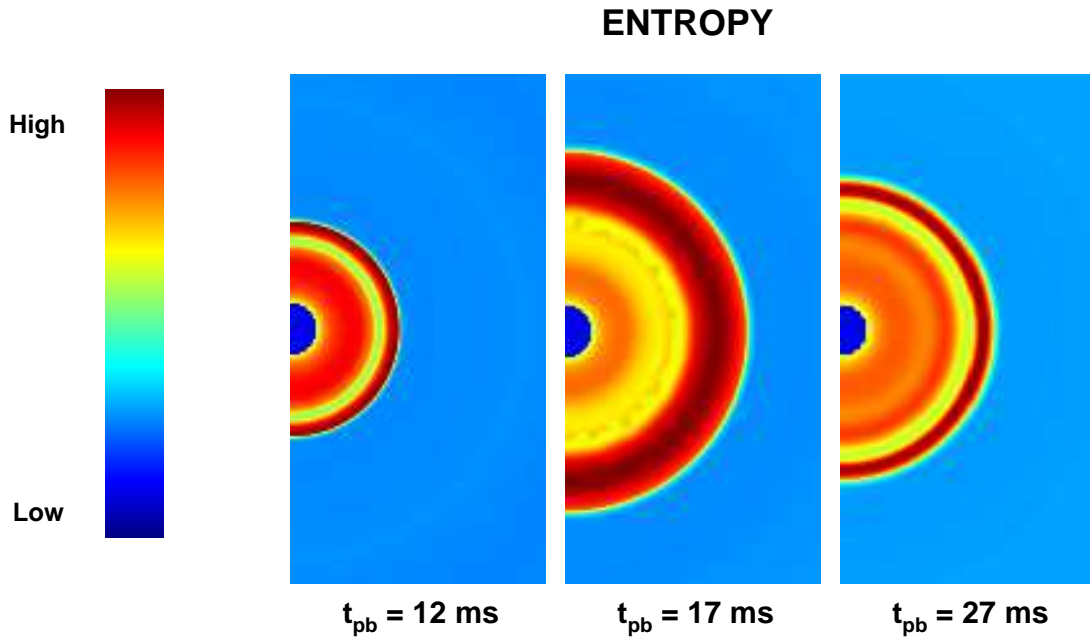


Fig. 7a.— Two-dimensional plots showing the entropy evolution of the $25 M_{\odot}$ model in a “low-test” simulation with neutrino transport (simulation G).

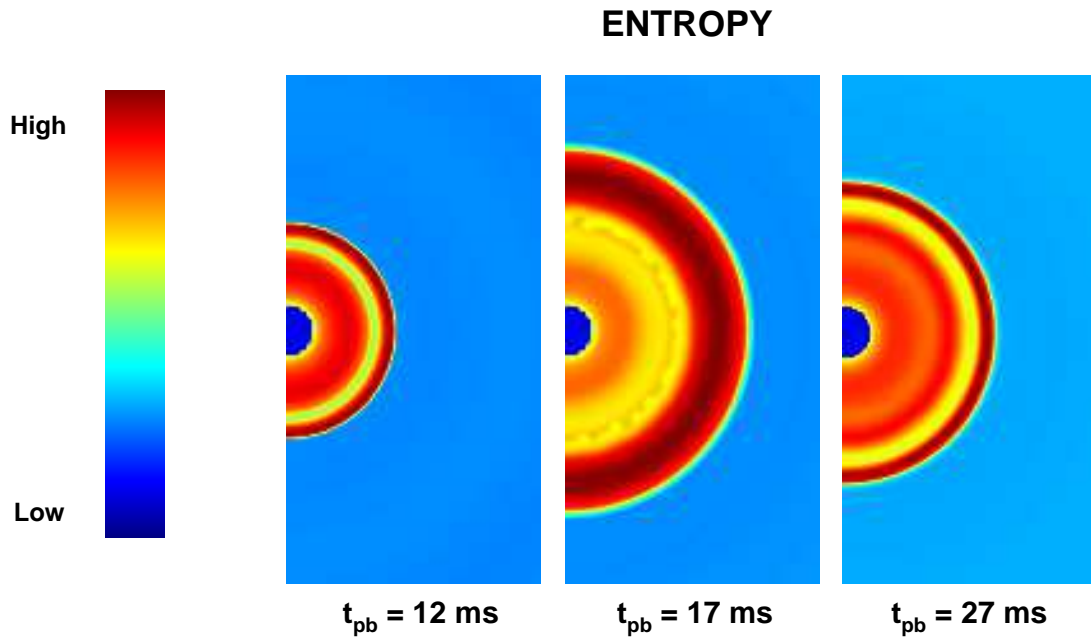


Fig. 8a.— Two-dimensional plots showing the entropy evolution of the $25 M_{\odot}$ model in a “low-test” simulation with neutrino transport that includes “finite-time” effects (simulation H).

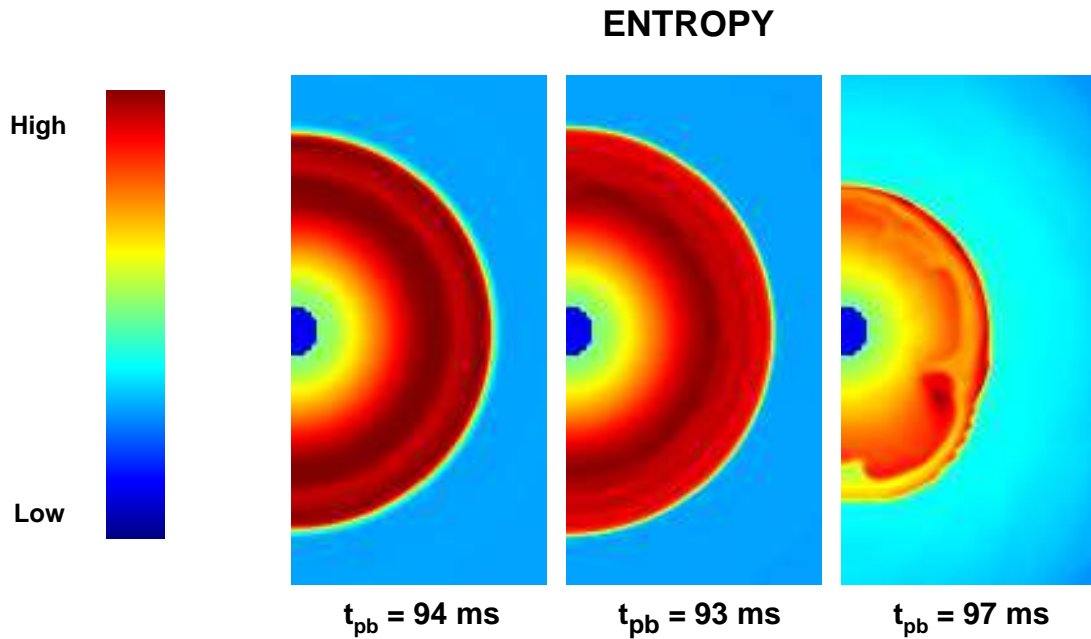


Fig. 9.— Two-dimensional entropy plots from simulations D, E, and G, at “late” times.

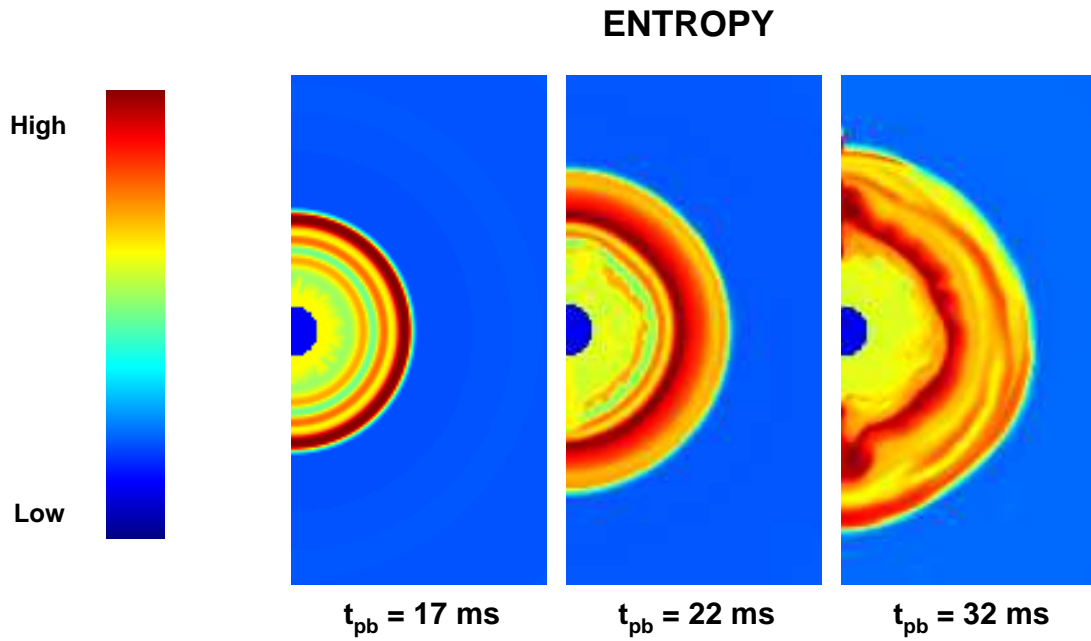


Fig. 10a.— Two-dimensional plots showing the entropy evolution of the $15 M_{\odot}$ model in a simulation without neutrino transport (simulation K).

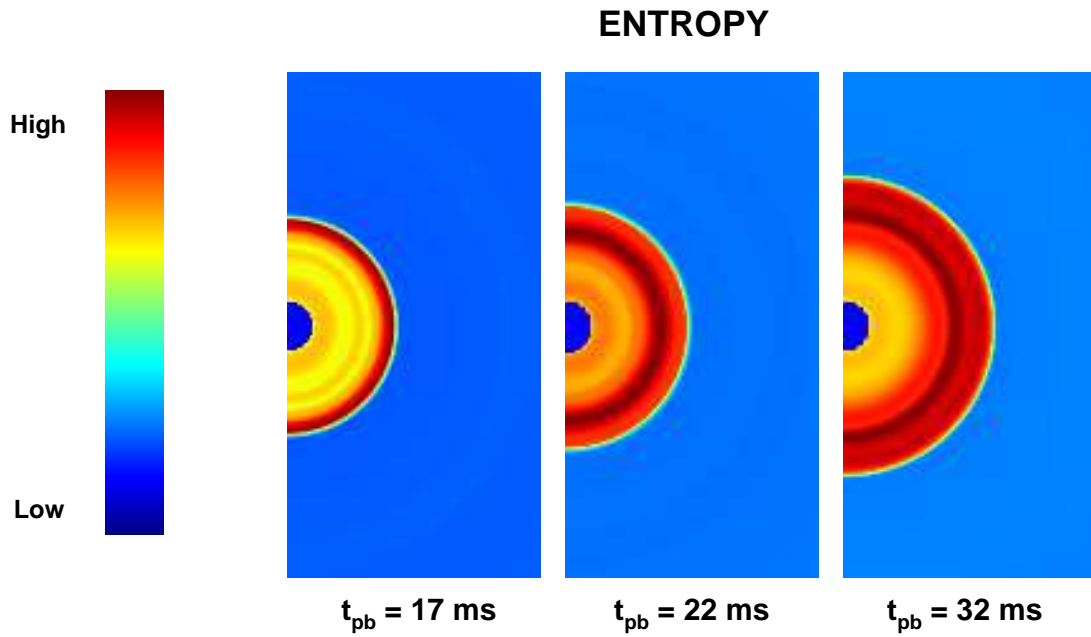


Fig. 11a.— Two-dimensional plots showing the entropy evolution of the $15 M_{\odot}$ model in a simulation with neutrino transport (simulation L).

The Interplay Between Protoneutron Star Convection and Neutrino Transport in Core Collapse Supernovae

A. Mezzacappa^{1,2}, A. C. Calder^{1,3}, S. W. Bruenn⁴, J. M. Blondin⁵,
M. W. Guidry^{1,2}, M. R. Strayer^{1,2}, and A. S. Umar³

Accepted for publication in *The Astrophysical Journal*

¹Theoretical and Computational Physics Group, Oak Ridge National Laboratory, Oak Ridge,
TN 37831-6354

²Department of Physics and Astronomy, University of Tennessee, Knoxville, TN 37996-1200

³Department of Physics and Astronomy, Vanderbilt University, Nashville, TN 37235

⁴Department of Physics, Florida Atlantic University, Boca Raton, FL 33431-0991

⁵Department of Physics, North Carolina State University, Raleigh, NC 27695-8202

Abstract

We couple two-dimensional hydrodynamics to realistic one-dimensional multigroup flux-limited diffusion neutrino transport to investigate protoneutron star convection in core collapse supernovae, and more specifically, the interplay between its development and neutrino transport. Our initial conditions, time-dependent boundary conditions, and neutrino distributions for computing neutrino heating, cooling, and deleptonization rates are obtained from one-dimensional simulations that implement multigroup flux-limited diffusion and one-dimensional hydrodynamics.

The development and evolution of protoneutron star convection are investigated for both 15 and 25 M_{\odot} models, representative of the two classes of stars with compact and extended iron cores, respectively. For both models, in the absence of neutrino transport, the angle-averaged radial and angular convection velocities in the initial Ledoux unstable region below the shock after bounce achieve their peak values in ~ 20 ms, after which they decrease as the convection in this region dissipates. The dissipation occurs as the gradients are smoothed out by convection. This initial protoneutron star convection episode seeds additional convectively unstable regions farther out beneath the shock. The additional protoneutron star convection is driven by successive negative entropy gradients that develop as the shock, in propagating out after core bounce, is successively strengthened and weakened by the oscillating inner core. The convection beneath the shock distorts its sphericity, but on the average the shock radius is not boosted significantly relative to its radius in our corresponding one-dimensional models.

In the presence of neutrino transport, protoneutron star convection velocities are too small relative to bulk inflow velocities to result in any significant convective transport of entropy and leptons. This is evident in our two-dimensional entropy snapshots, which in this case appear spherically symmetric. The peak angle-averaged radial and angular convection velocities are orders of magnitude smaller than they are in the corresponding “hydrodynamics only” models.

A simple analytical model supports our numerical results, indicating that the inclusion of neutrino transport reduces the entropy-driven (lepton-driven) convection growth rates and

asymptotic velocities by a factor ~ 3 (50) at the neutrinosphere and a factor ~ 250 (1000) at $\rho = 10^{12}$ g/cm³, for both our 15 and 25 M_{\odot} models. Moreover, when transport is included, the initial postbounce entropy gradient is smoothed out by neutrino diffusion, whereas the initial lepton gradient is maintained by electron capture and neutrino escape near the neutrinosphere. Despite the maintenance of the lepton gradient, protoneutron star convection does not develop over the 100 ms duration typical of all our simulations, except in the instance where “low-test” initial conditions are used, which are generated by core collapse and bounce simulations that neglect neutrino–electron scattering and ion–ion screening corrections to neutrino–nucleus elastic scattering.

Models favoring the development of protoneutron star convection either by starting with more favorable, albeit artificial (“low-test”), initial conditions or by including transport corrections that were ignored in our “fiducial” models were considered. Our conclusions nonetheless remained the same. Evidence of protoneutron star convection in our two-dimensional entropy snapshots was minimal, and as in our “fiducial” models, the angle-averaged convective velocities when neutrino transport was included remained orders of magnitude smaller than their counterparts in the corresponding “hydrodynamics only” models.

Subject headings: (stars:) supernovae: general – convection

1. Introduction

1.1. Current Core Collapse Supernova Paradigm

The current core collapse supernova paradigm begins with the collapse of the iron core of an evolved massive star at the end of its thermonuclear evolution. The rebound of the inner core, brought about by the rapid increase of pressure with density when the density rises above nuclear matter density, generates a shock wave at a radius ~ 20 km, and drives it into the outer core. All groups currently agree that, rather than propagating directly outward through the entire envelope and producing a supernova, the shock stalls and turns into an accretion shock at a radius of 100 – 200 km. This happens for several reasons: (1) Nuclear dissociation behind the shock lowers the ratio of pressure to energy, thereby lowering the strength of the shock for a given energy delivered to it by the inner core. (2) There is a reduction in both the thermal and lepton number contribution to the shock pressure as a result of the intense burst of ν_e radiation through the shock that ensues when it passes outwardly through the ν_e -sphere, which at this time is located at ~ 60 km.

All groups also currently believe that the supernova is powered by some variant of the “shock reheating mechanism” of Wilson (1985) and Bethe and Wilson (1985). In this mechanism, the material behind the shock heats on a time scale of hundreds of milliseconds by the transfer and deposition of energy by neutrinos from the hot contracting core. As a result of this energy transfer, the shock is once again driven out. This is in contrast to the original neutrino-driven supernova mechanism of Colgate and White (1966), which operated on the dynamical time scale of milliseconds.

The energy transfer between neutrinos and matter behind the shock is mediated primarily by the charged current reactions $\nu_e + n \rightleftharpoons p + e^-$ and $\bar{\nu}_e + p \rightleftharpoons n + e^+$. When these reactions proceed to the right, the matter heats; when they proceed to the left, the matter cools. To drive these reactions sufficiently rapidly to the right for a supernova to develop requires a critical combination of ν_e - $\bar{\nu}_e$ luminosity and RMS energy (*e.g.*, Burrows and Goshy 1993) that no recent realistic,

spherically symmetric, numerical simulation has to date delivered (Bruenn 1993; Cooperstein 1993; Wilson and Mayle 1993).

1.2. Role of Fluid Instabilities

A possible way out of this impasse is illuminated by the early recognition that neutrino luminosities and RMS energies might be enhanced by fluid instabilities occurring below the neutrinosphere (Epstein 1979; Bruenn, Buchler, and Livio 1979; Colgate and Petschek 1980; Mayle 1985; Wilson *et al.* 1986; Arnett 1987; Burrows 1987; Burrows and Lattimer 1988), or that the neutrino energy deposition efficiency might be increased by fluid instabilities occurring above the neutrinosphere (Bethe 1990; Herant, Benz, and Colgate 1992; Colgate, Herant, and Benz 1993). Both of these possibilities are being vigorously pursued by a number of groups. Additional motivation for the study of fluid instabilities at this early stage in the development of a supernova is the existence of a large variety of observational hints that large-scale mixing processes occurred in the early phase of the explosion of SN 1987A, and played an important role in generating the observables (*e.g.*, see Herant, Benz, and Colgate 1992, 1994; Burrows, Hayes, and Fryxell 1995; Janka and Müller 1996).

1.3. Fluid Instabilities below the Neutrinosphere

Consider the region in the vicinity of and below the neutrinosphere, which will be the subject of this paper. Material in this region is in nuclear statistical equilibrium, and its thermodynamic state and composition can therefore be specified by just three independent variables. We will choose these to be the dimensionless entropy per baryon, s , the lepton fraction, Y_ℓ , and the pressure, P . Above the neutrinosphere, electrons and neutrinos are no longer strongly interacting and Y_ℓ should be replaced by the electron fraction, Y_e . In the presence of gradients in s and/or Y_ℓ , a strong gravitational field, and the neutrino transport of energy and leptons, the material may be unstable to any one of a number of fluid instabilities (Bruenn and Dineva 1996). If we ignore the

effects of neutrino transport for the moment, the situation simplifies and the number of possible fluid instabilities is reduced to one, *viz.*, the Rayleigh-Taylor (convective) instability. Under these conditions, the criterion for convective instability is the “Ledoux” condition, given by

$$\left(\frac{\partial \rho}{\partial \ln Y_\ell}\right)_{s,P} \left(\frac{\partial \ln Y_\ell}{\partial r}\right) + \left(\frac{\partial \rho}{\partial \ln s}\right)_{Y_\ell,P} \left(\frac{\partial \ln s}{\partial r}\right) > 0 \quad (1)$$

The derivative $\left(\frac{\partial \rho}{\partial \ln s}\right)_{Y_\ell,P}$ is negative for all thermodynamic states; therefore, negative entropy gradients always tend to be destabilizing. On the other hand, the derivative $\left(\frac{\partial \rho}{\partial \ln Y_\ell}\right)_{s,P}$ is negative for large Y_ℓ , but becomes positive for small Y_ℓ .⁶ The critical value of Y_ℓ at which the derivative changes sign depends on s and P , but is typically in the range 0.1 – 0.2. Thus, negative gradients in Y_ℓ initially tend to be destabilizing, but become stabilizing when the core deleptonizes sufficiently for values of Y_ℓ to go below the critical value. We will refer to convection driven by negative gradients in s and Y_ℓ near and below the neutrinosphere as “entropy-driven protoneutron star convection” and “lepton-driven protoneutron star convection,” respectively. These modes of convection are to be distinguished from the entropy-driven convection that occurs above the neutrinosphere after shock stagnation. This convection is sustained by neutrino heating, and will be referred to as “neutrino-driven convection.” It will be the subject of another paper (Mezzacappa *et al.* 1997; see also, Herant *et al.* 1992, 1994, Miller *et al.* 1993, Burrows *et al.* 1995, and Janka and Müller 1996).

⁶An increase in Y_ℓ implies an increase in the number of particles, and this must be accompanied by a decrease in the temperature T to keep s constant. The increase in particle number tends to increase P , while the decrease in temperature tends to decrease P . At large Y_ℓ , the increase in the number of particles has the more important effect on P , and ρ must decrease to keep P constant. Under these conditions, the derivative $\left(\frac{\partial \rho}{\partial \ln Y_\ell}\right)_{s,P}$ is therefore negative. At small Y_ℓ , the decrease in temperature is the more important effect, and ρ must increase to keep P constant, making the derivative positive.

If we now bring the neutrino transport of energy and leptons into the picture, entropy- and lepton-driven protoneutron star convection are still possible (with reduced growth rates), and two additional modes of instability, “neutron fingers” and “semiconvection,” become possible. [See Bruenn and Dineva (1996) for a physical description of these instabilities.] These instabilities occur on a diffusion rather than on a dynamical time scale, and usually require that one of the gradients (s or Y_ℓ) be stabilizing while the other be destabilizing, and that energy and lepton equilibration by neutrinos proceed at different rates.

There are several reasons why fluid instabilities in the region below the neutrinosphere may play an important role in the shock reheating mechanism. All have to do with the fact that instabilities tend to drive fluid motions that tend to circulate the fluid throughout the unstable region. The fluid motions associated with entropy-driven protoneutron star convection will tend to advect high-entropy material from deeper in the core to the vicinity of the neutrinosphere, increasing the temperature of the neutrinosphere and thereby increasing both the ν_e and the $\bar{\nu}_e$ emission rates. Lepton-driven protoneutron star convection will tend to advect lepton-rich material from deeper in the core to the vicinity of the neutrinosphere, increasing and decreasing the ν_e and $\bar{\nu}_e$ emission rates, respectively, and hastening the deleptonization of the core.

1.4. Lepton-Driven Convection

As we will indicate below, if protoneutron star convection is important for shock reheating, lepton-driven protoneutron star convection is probably more important than entropy-driven protoneutron star convection. A negative lepton gradient results from the fact that the region well below the neutrinosphere is lepton rich relative to the material flowing inward through the neutrinosphere at the time of shock stagnation. This is because the latter is completely shock dissociated into free neutrons and protons and is hydrostatically settling onto the core when it passes through the neutrinosphere. Electron capture therefore proceeds rapidly on the plethora of free protons, and plenty of time is available for the ν_e ’s produced by these electron captures to escape. Thus, the material in the vicinity of the neutrinosphere at this time is very lepton

poor ($Y_\ell \lesssim 0.1$). On the other hand, material deep within the core passed rapidly through the neutrinosphere during infall, and either never encountered the shock, or encountered the shock below the neutrinosphere, as the shock was beginning to form. This material was therefore “cold,” and contained only a small mass fraction of free protons when it passed inwardly through the neutrinosphere. As a result, electron capture proceeded more slowly and the ν_e ’s produced by the electron capture had less time to escape. Consequently, the material residing deep within the core has a higher lepton fraction ($Y_\ell \sim 0.3$) at the time of shock stagnation. A negative gradient in Y_ℓ below the neutrinosphere is thus naturally established after shock stagnation, and this gradient is maintained by continuing deleptonization near the neutrinosphere.

The negative gradient in Y_ℓ , unless stabilized by a positive gradient in s , will drive a convective flow that may advect leptons from the lepton-rich interior to the vicinity of the neutrinosphere, where they will be radiated away as ν_e ’s. This is the basis of the original suggestion of Epstein (1979), and the early work of Bruenn, Buchler, and Livio (1979), Colgate and Petschek (1980), and Livio, Buchler and Colgate (1980). Interest in this early work waned when it was pointed out that the positive entropy gradient established by reenergizing the shock would stabilize much of this region (Lattimer and Mazurek 1981; Smarr *et al.* 1981), and because of the growing interest in the “prompt” supernova mechanism. However, as the prompt mechanism proved untenable and attention turned to shock reheating, and as SN 1987A appeared with its many hints of fluid instabilities occurring early on, interest in the role of fluid instabilities in the supernova mechanism revived (Arnett 1986, 1987; Bethe 1990, 1993; Bruenn and Mezzacappa 1994; Bruenn, Mezzacappa, and Dineva 1995; Bruenn and Dineva 1996; Burrows 1987; Burrows and Lattimer 1988; Burrows and Fryxell 1992, 1993; Burrows, Hayes and Fryxell 1995; Colgate, Herant, and Benz 1993; Herant, Benz, and Colgate 1992; Herant *et al.* 1994; Janka and Müller 1993a, 1993b, 1995, 1996; Müller 1993; Müller and Janka 1994; Shimizu, Yamada, and Sato 1993, 1994; Wilson and Mayle 1988, 1993).

1.5. Neutron Fingers

The stabilizing effect of the positive entropy gradient established by the shock as it gathers power from the rebounding inner core prompted Mayle and Wilson to invoke neutron fingers as a driver of fluid circulation below the neutrinosphere (Mayle 1985, Wilson *et al.* 1986, Wilson and Mayle 1988, 1993). Modeling the fluid circulation by a mixing-length algorithm, they found that if the fluid circulation were made sufficiently vigorous, they could generate explosions out of what would otherwise have been duds. Neutron fingers can occur in the presence of a positive entropy gradient and a negative lepton gradient if the energy equilibration rate of a fluid element with the background is faster than the lepton equilibration rate. The opposite was found to be the case, however, in recent investigations by Bruenn, Mezzacappa and Dineva (1995), and Bruenn and Dineva (1996). The implication of these investigations is that the material, if unstable at all, will be unstable to semiconvection rather than neutron fingers. Semiconvection tends to drive more localized flows and consequently may not transport leptons efficiently to the neutrinosphere.

1.6. Entropy-Driven Convection

While the shock establishes a positive entropy gradient as it gathers strength, Arnett (1986, 1987) pointed out that the dissipation of the shock farther out, due to nuclear dissociation and ν_e radiation, will imprint a negative entropy gradient and therefore destabilize this region to entropy-driven convection. While Arnett (1986, 1987), Burrows (1987), and Burrows and Lattimer (1988) emphasized the importance of neutrinosphere heating by this convection, the latter two papers pointed out that the transfer of heat to the neutrinosphere from an entropy spike deeper in the core can accelerate mantle collapse and thereby inhibit the outward progress of the shock (see also Bethe, Brown, and Cooperstein 1987).

For entropies exceeding ~ 5 , a negative gradient in $\ln s$ is more destabilizing than a negative gradient in $\ln Y_\ell$ of the same magnitude (*e.g.*, Bruenn, Mezzacappa, and Dineva 1995, Fig. 1); therefore, one might expect a vigorous entropy-driven protoneutron star convection to become

established exterior to $0.7 - 1.0 M_{\odot}$ immediately after shock propagation. However, the magnitude and location of the negative entropy gradients established by the dissipating shock depends sensitively on the numerical model used to compute the prior evolution of the core (Bruenn and Mezzacappa 1994, Fig. 1). The more realistic the numerical model, the smaller the magnitude of the negative entropy gradients established by the shock. It is therefore likely that both the magnitude and the extent of the negative entropy gradients established by the shock will be minimal. Once entropy-driven protoneutron star convection gets established, the convective mixing will tend to flatten the entropy gradient driving it; there is no process maintaining the negative entropy gradient, and the force driving entropy-driven convection will dissipate. Thus, entropy-driven protoneutron star convection sows the seeds of its own destruction. A final problem with entropy-driven protoneutron star convection for shock revival is that numerical simulations indicate that conditions favorable for shock revival are not established until ~ 50 ms after bounce (Janka and Müller 1993a; Bruenn and Mezzacappa 1994). On the other hand, multidimensional simulations of entropy-driven protoneutron star convection show that the convection quickly grows into the nonlinear regime (10 - 15 ms), and the entropy gradients are flattened in $\sim 25 - 30$ ms (Burrows and Fryxell 1992, 1993; Janka and Müller 1993b, 1996; Müller 1993; Müller and Janka 1994). Thus, by the time the region above the neutrinosphere is in a configuration favorable for neutrino energy deposition, entropy-driven protoneutron star convection has dissipated. It is therefore unlikely that it will revive the shock. However, it may play a role in seeding both lepton-driven protoneutron star convection and neutrino-driven convection. It will also affect the structure of the core, and should not be ignored.

1.7. Current Status of Protoneutron Star Convection

The role played by entropy- and lepton-driven protoneutron star convection in the supernova mechanism and the evolution of the core is highly unclear and contradictory at the present time. Burrows and Fryxell (1992) found vigorous entropy-driven protoneutron star convection in 2-D hydrodynamics computations that did not include neutrino transport. With the inclusion of

radial-ray neutrino diffusion they found a “convective trigger,” *i.e.*, convectively enhanced neutrino luminosities that triggered an explosion within 20 ms (Burrows and Fryxell 1993). In a later work (Burrows, Hayes, and Fryxell 1995), they report that entropy- and lepton-driven protoneutron star convection are “weak,” and presumably unimportant. Herant *et al.* (1994), using an SPH hydrodynamics method, found intermittent and model-dependent lepton-driven convection in a relatively narrow region in the vicinity of the neutrinosphere, and entropy-driven convection farther out — the latter ultimately merging with neutrino-driven convection. Janka and Müller (1993b, 1996), Müller (1993), and Müller and Janka (1994) performed 2- and 3-D hydrodynamics simulations of protoneutron star convection with several postcollapse models and found that the convection, while model dependent, is initially vigorous in all cases. In their most recent work they report that convection’s purely hydrodynamic effect pushes the shock from its stagnation radius at ~ 200 km (one-dimensional initial conditions) out to ~ 400 km (two-dimensional case) and to ~ 300 km (three-dimensional case). Keil, Janka, and Müller (1996) have recently followed the evolution of a protoneutron star for more than 1 s with 2-D hydrodynamics and radial-ray neutrino diffusion. They found that lepton-driven Ledoux convection continues for a long time and engulfs the entire core after about 1 s. Moreover, they found that the convection increases the neutrino luminosities by up to a factor of 2 and the mean energies of the emitted neutrinos by 10–20%. Bruenn and Mezzacappa (1994) performed self-consistent 1-D simulations of protoneutron star evolution using multigroup flux-limited diffusion (MGFLD) for neutrino transport and a mixing-length algorithm for convection. In contrast to the results of Janka and Müller, they found only mild convective activity inside and around the neutrinosphere for a duration ~ 30 ms, although their simulations covered a postbounce period of 0.5 s. While one may argue that the mixing-length approximation fails to reproduce all of the properties of the convective flow, it is nevertheless sensitive to any Ledoux instabilities, and would trace out these instabilities as they develop.

1.8. This Work

Part of the reason for the present confusion concerning the vigor and extent of protoneutron star convection and its role in the supernova mechanism is that numerically simulating this convection is a very difficult problem in radiation hydrodynamics. Neutrinos and matter are strongly coupled in this regime, and it can be expected that neutrino transport will have a profound influence on both the character and the growth rate of any fluid instability. Different initial postcollapse models and alternative approximations to the neutrino transport can produce widely varying results. A self-consistent calculation of protoneutron star convection requires that both the hydrodynamics and the neutrino transport be multidimensional. Only Herant *et al.* (1994) have performed such calculations, although their neutrino transport was much simpler than the transport used in sophisticated 1-D codes. Helpful insights into the nature and growth rates of fluid instabilities in this regime can be obtained by semianalytical investigations that are now in progress (Bruenn and Dineva 1997).

In this paper we investigate protoneutron star convection with a numerical scheme that is a vast improvement over the 1-D scheme used by Bruenn and Mezzacappa (1994). Here we couple 2-D PPM hydrodynamics with sophisticated 1-D MGFLD. Computations of protoneutron star convection that ignore neutrino transport or that implement radial-ray neutrino transport ignore the tendency of transport to equilibrate upflows and downflows with each other in energy and leptons, thus reducing the very buoyancy contrast driving these flows. We show by a simple analytical example that these computations therefore overestimate the growth rates and final amplitude of protoneutron star convection. Our 1-D neutrino transport represents an alternative intermediate step (compared with radial-ray neutrino transport) along the way to full multidimensional transport. 1-D transport obtains in the limit in which the neutrino transport in the tangential direction is rapid enough to render the neutrino fields spherically symmetric, and therefore, in this regard, is complementary to radial-ray transport. It is also important to note that our neutrino transport is multigroup, rather than gray, which becomes particularly important near the neutrinospheres, where the matter becomes semitransparent to neutrinos and where gray

transport would not be adequate.

In Section 2, we describe our hydrodynamics code, “EVH-1,” our procedure coupling neutrino transport to EVH-1, and the models used to initiate the simulations. In Section 3 we present the results of our simulations. The tendency of energy and lepton transport by neutrinos to suppress protoneutron star convection, which is the central feature in all of our numerical results, is discussed with the aid of a simple analytical model in Section 4. A summary of our work and of its implications is given in Section 5.

2. Initial Models and Methodology

2.1. Overview

In this work all simulations begin with either the $15 M_{\odot}$ or the $25 M_{\odot}$ precollapse models, S25s7b or S15s7b, provided by Woosley (Woosley & Weaver 1995, Weaver & Woosley 1997). These initial models were evolved through core collapse and bounce using MGFLD neutrino transport and one-dimensional Lagrangian hydrodynamics (Bruenn 1985). These 1-D simulations were continued approximately 700 milliseconds after bounce for the purpose of generating boundary and neutrino distribution data to be used in our 2-D simulations, as described below. At a simulation time of typically tens of milliseconds after bounce, the one-dimensional configurations were mapped onto a two-dimensional Eulerian grid. The inner and outer boundaries of the two-dimensional grid were chosen to be at radii of 20 km and 1000 km, respectively, for all runs. These choices set the inner and outer boundaries well below and above the unstable regions at the onset of the simulations. The grids used 128 nonuniform radial spatial zones. This gave sufficient resolution at the inner boundary and at the shock. The nonuniform zoning was varied until, for a test simulation, excellent agreement was seen between one-dimensional runs using 128 nonuniform and 512 uniform zones (see Figures 2c–d). 128 uniform angular zones spanning a range of 180 degrees were used for θ . With the assumption of axisymmetry, the range of 180 degrees spans the entire physical space, and accordingly, reflecting boundary conditions are used on the polar axis.

Because the finite differencing in our PPM scheme is nearly noise free, and because we cannot rely on machine roundoff to seed convection in a time that is short compared with the hydrodynamics time scales in our runs, we seeded convection in the Ledoux unstable regions below and around the neutrinospheres by applying random velocity perturbations to the radial and angular velocities between $\pm 5\%$ of the local sound speed. This is consistent with seeding used by other groups. Moreover, in a 2-D simulation of convection during the shell burning of oxygen prior to core collapse, Bazan and Arnett (1994) found inhomogeneities of density, temperature, pressure, and electron fraction $\sim 5\%$, 1% , 3% , and 0.08% , respectively, and convection velocities

$\sim 15\%$ of the local sound speed. Therefore, our seeding choice seems reasonable, although a more systematic study should be carried out.

The two-dimensional hydrodynamics was evolved using EVH-1, an extended version of the PPM hydrodynamics code VH-1. One of the extensions allows for coupling to general equations of state. For the most part, matter in our simulations is in nuclear statistical equilibrium (NSE), and to describe its thermodynamic state we used the equation of state provided by Lattimer and Swesty (Lattimer & Swesty 1991). However, below a density and temperature threshold, the code switches to a non-NSE equation of state. If a zone falls below the density or temperature threshold of $1.674 \times 10^7 \text{ g cm}^{-3}$ or 0.3447 MeV , respectively, it is “deflashed” to silicon, while conserving energy within the zone. This is well outside the convectively unstable region, and deflashing was therefore performed in a spherically symmetric manner. An ideal gas equation of state, plus internal degrees of freedom to mimic the NSE equation of state and to provide a more seamless transition to non-NSE, is then used to describe the silicon in its subsequent evolution. As will be described in detail later, with both equations of state, tables of thermodynamic quantities are constructed at the beginning of a simulation, and as the calculation proceeds, the code interpolates within these tables.

At each time step in the two-dimensional evolution, the results of the corresponding one-dimensional MGFLD run, completed at a prior time, provide spherically symmetric time-dependent boundary data for our inner and outer two-dimensional boundaries, and neutrino distributions for the local neutrino heating, cooling, and matter deleptonization everywhere on our two-dimensional grid. The boundary data consist of enclosed mass, radial velocity, density, temperature, electron fraction, pressure, and specific internal energy, and values at our fixed inner Eulerian radius were extracted from the one-dimensional Lagrangian data by interpolation in r and t . A call to the equation of state provides the boundary value of the first adiabatic index, which is required by our PPM scheme. The outer boundary data were specified in the same way. The neutrino heating and cooling, and the matter deleptonization, were computed at each time step using tables of ψ_i^0 's in r , t , and E_ν , constructed from our one-dimensional simulations.

$[\psi_i^0(r, t, E_\nu)]$ are the zeroth moments of the neutrino distribution functions; i is a neutrino flavor index.] Ideally, the neutrino-matter momentum transfer should also be included. However, this is a small correction to the matter pressure.

Gravity was assumed to be Newtonian and spherically symmetric in our two-dimensional simulations. The justification for the latter is the fact that the gravitationally unstable region was dominated by the spherically symmetric enclosed mass at the region’s base. The time dependence of the mass enclosed by our inner boundary, given by our one-dimensional MGFLD runs, was taken into account. The contribution to the gravitational field of the mass on the grid was calculated at each time step by finding the angle-averaged density in a shell between radial grid points, and summing the masses of the shells up to a particular radial grid point. (The solution of the Poisson equation for the gravitational potential will be incorporated in future investigations.)

Comparisons were made (see below) to ensure that in one dimension the results from our code matched the results obtained with the MGFLD code, modulo EVH-1’s better resolution of the shock.

2.2. Details of the Simulations

Table 1 contains the initial times for, and a brief description of, each simulation. All of the simulations listed below were performed with the PPM code, and began a few milliseconds after bounce. The one-dimensional PPM simulations were performed for the purpose of comparison with our one-dimensional MGFLD simulations.

In simulations B, D, J, and L, the electron neutrino and electron antineutrino distributions ($\psi_{\nu_e, \bar{\nu}_e}^0$) used to compute the local neutrino heating, cooling, and matter deleptonization are generated by our accompanying one-dimensional simulations that include all neutrino flavors and interactions — neutrino–electron scattering (NES) and ion–ion screening corrections included.

Simulations F, G, and H were initiated from a model whose prior evolution involved a less rigorous treatment of neutrino transport, and were dubbed our “low-test” runs. In particular, the

initial model for these runs was evolved through bounce by the MGFLD code, neglecting NES and ion–ion screening corrections. This less rigorous treatment of neutrino transport provides initial conditions for the two-dimensional simulations that are more conducive to the development of protoneutron star convection because a larger entropy gradient is established by the weakening of an originally stronger shock.

To explain the way the neutrino distributions are used to calculate the local neutrino heating, cooling, and deleptonization, we must describe how EVH-1 carries out the simulations:

EVH-1 performs the hydrodynamics evolution in sweeps over the grids. In the one-dimensional case, there is a sweep in the radial direction. In the two-dimensional case, there is a sweep first in the radial direction for each angle and then in the angular direction for each radius. In a particular sweep, there are four principal variables that evolve. These are density (ρ), temperature (T), electron fraction (Y_e), and specific internal energy (ϵ). (Y_e in a zone changes due to hydrodynamic advection, in addition to transformations between e^- 's, e^+ 's, ν_e 's, and $\bar{\nu}_e$'s.) In order to update these quantities, thermodynamic quantities such as the pressure are required. In order to calculate these quantities, EVH-1 calculates tables of state variables and interpolates within these tables. The three-dimensional tables are constructed such that ρ , T , and Y_e are the independent variables, and tables are constructed for ϵ , pressure (P), entropy (s), and other variables. For the combination ρ , T , and Y_e in a given zone of our two-dimensional grid, the code performs linear interpolations using the logarithms of both the independent (*e.g.*, ρ) and the dependent (*e.g.*, P) variables in our table to obtain the corresponding dependent variables for that zone. For details of the interpolation scheme, see Mezzacappa and Bruenn (1993).

Because the hydrodynamics evolution updates ρ , ϵ , and Y_e , it is necessary to update T by iteration of

$$\Delta T = \frac{\epsilon^{\text{hyd}} - \epsilon^{\text{int}}}{\left(\frac{\partial \epsilon}{\partial T}\right)_{\rho, Y_e}}, \quad (2)$$

where ϵ^{hyd} and ϵ^{int} are the specific internal energy (a) partially updated by the hydrodynamics and (b) given by the interpolation, respectively; and $\left(\frac{\partial\epsilon}{\partial T}\right)_{\rho,Y_e}$ is the specific heat. ϵ^{int} and $\left(\frac{\partial\epsilon}{\partial T}\right)_{\rho,Y_e}$ are evaluated at the current iterate, T^0 . The iterations occur until ΔT falls below a specified tolerance.

The sweep proceeds by first calling the interpolation routine to update T , and then calculates variables such as P and s in each zone of a one-dimensional sweep. Next, the sweep proceeds by calling the PPM routines for the hydrodynamics evolution, partially updating ρ , ϵ , and Y_e . Then, the simulations make use of the MGFLD neutrino data in an operator split manner to fully update ϵ and Y_e according to the prescriptions below. The next sweep repeats this procedure, first updating T , then evolving the hydrodynamics, and further updating ϵ and Y_e due to neutrino emission and absorption.

In simulations B, D, F, and L, the neutrino heating and cooling, and the change in the electron fraction, were computed at each time step within each angular sweep (i.e., at a given radius) using the following formulae:

$$\partial\epsilon/\partial t = c \sum_{i=1}^2 \int E_\nu^3 dE_\nu [\psi_i^0/\lambda_i^{(a)} - j_i(1 - \psi_i^0)]/\rho(hc)^3, \quad (3)$$

and

$$\partial Y_e/\partial t = cm_B \sum_{i=1}^2 \alpha_i \int E_\nu^2 dE_\nu [\psi_i^0/\lambda_i^{(a)} - j_i(1 - \psi_i^0)]/\rho(hc)^3, \quad (4)$$

where E_ν , ψ_i^0 , $\lambda_i^{(a)}$, and j_i are the electron neutrino or antineutrino energy, zeroth distribution function moment, absorption mean free path, and emissivity, respectively; m_B is the baryon mass; $i = 1, \alpha_1 = 1$ corresponds to electron neutrinos, and $i = 2, \alpha_2 = -1$ corresponds to electron antineutrinos. As mentioned earlier, the time-dependent ψ_i^0 's are obtained from tables in r , t , and

E_ν constructed from our one-dimensional MGFLD simulations.

Simulations E and H made use of modified versions of the above formulae to account for the “finite time” required for transport of neutrinos between an element of convecting material and its background. The corrected heating rate is calculated from the above heating rate by considering the mean free paths and by calculating a minimum transport time, which is then used to calculate a correction factor. The mean free path, $\lambda(r, E_\nu, i)$, is calculated from the emission, absorption, and isoenergetic scattering mean free paths for each radius (r), neutrino energy group (E_ν), and for each neutrino type (i). Once $\lambda(r, E_\nu, i)$ is determined, the diffusion time, $t_{\text{diff}}(r, E_\nu, i)$, is calculated by

$$t_{\text{diff}}(r, E_\nu, i) = \frac{(r_{\text{scale}})^2}{c\lambda(r, E_\nu, i)} \quad (5)$$

where r_{scale} is the length scale of a convecting element. In these calculations, this scale was taken to be 10 km, which is about one pressure scale height in the convectively unstable region of the core, 10 to 100 ms after bounce. The free escape time, $t_{\text{esc}}(r, E_\nu, i)$, represents the minimum transport time of neutrinos from the convecting element, and is given by

$$t_{\text{esc}}(r, E_\nu, i) = \frac{r_{\text{scale}}}{c} . \quad (6)$$

The free escape time is a physical limit, and it must be used when $t_{\text{diff}}(r, E_\nu, i)$ becomes so small, i.e., $\lambda(r, E_\nu, i)$ becomes so large, that it would imply that neutrinos are propagating faster than the speed of light. The quantity $t_{\text{trans}}(r, E_\nu, i)$ smoothly interpolates between $t_{\text{diff}}(r, E_\nu, i)$ [small $\lambda(r, E_\nu, i)$] and $t_{\text{esc}}(r, E_\nu, i)$ [large $\lambda(r, E_\nu, i)$], and is given by

$$t_{\text{trans}}(r, E_\nu, i) = \left[(t_{\text{diff}}(r, E_\nu, i))^2 + (t_{\text{esc}}(r, E_\nu, i))^2 \right]^{1/2} . \quad (7)$$

This expression tends to weight preferentially the larger of $t_{\text{diff}}(r, E_\nu, i)$ and $t_{\text{esc}}(r, E_\nu, i)$. Next, from $[\partial\epsilon/\partial t](r, E_\nu, i)$, which is given by the individual terms in the integrand of equation (3), the heating time, $t_e(r, E_\nu, i)$, is given by

$$t_e(r, E_\nu, i) = \frac{\epsilon(r)}{[\partial\epsilon/\partial t](r, E_\nu, i)}. \quad (8)$$

The correction factor, c_{trans} , is then

$$c_{\text{trans}}(r, E_\nu, i) = \frac{t_e(r, E_\nu, i)}{t_e(r, E_\nu, i) + t_{\text{trans}}(r, E_\nu, i)}, \quad (9)$$

and the corrected heating rate becomes

$$(\partial\epsilon/\partial t)_{\text{corrected}} = c_{\text{trans}}(r, E_\nu, i)\partial\epsilon/\partial t. \quad (10)$$

A correction for the deleptonization rate is computed and applied in an analogous manner.

2.3. Initial Conditions

Table 2 contains the initial conditions for our simulations. The unstable region in the 25 M_\odot model, from which our “25 M_\odot ” simulations are initiated, extended from an enclosed mass of 0.82 M_\odot to an enclosed mass of 1.02 M_\odot for the case in which the prior evolution (up to postbounce) was calculated with comprehensive neutrino transport. For the “low-test” case, the region extended from an enclosed mass of 0.97 M_\odot to an enclosed mass of 1.21 M_\odot . For the 15

M_{\odot} model, from which our “15 M_{\odot} ” simulations are initiated, the unstable region extended from an enclosed mass of 0.79 M_{\odot} to an enclosed mass of 1.03 M_{\odot} .

3. Results

In Figure 1, we plot the initial entropy and electron fraction gradients for our 15 and 25 M_{\odot} models. In the 25 M_{\odot} case, we plot the gradients for both our original and “low-test” runs. Note that in the latter case there is a significantly larger initial entropy gradient. “Low-test” transport during core collapse leads to less deleptonization, and consequently, to a larger inner homologously collapsing core. As a result, at bounce a stronger shock forms (from a larger rebounding inner piston), and it forms farther out in radius. All are evident in the figure. For our original 25 M_{\odot} model, the neutrinospheres are initially located at (a) 71 km, (b) 63 km, and (c) 73 km for (a) electron neutrinos, (b) electron antineutrinos, and (c) muon and tau neutrinos and antineutrinos. For our “low-test” runs, the neutrinospheres are initially located at (a) 117 km, (b) 110 km, and (c) 119 km for (a) electron neutrinos, (b) electron antineutrinos, and (c) muon and tau neutrinos and antineutrinos. For our 15 M_{\odot} model, the neutrinospheres are initially located at (a) 68 km, (b) 59 km, and (c) 69 km for (a) electron neutrinos, (b) electron antineutrinos, and (c) muon and tau neutrinos and antineutrinos.

As a check that our inner and outer running boundary conditions and our procedure for computing the neutrino cooling, heating, and matter deleptonization rates are sufficient to ensure that 1-D EVH-1 simulations between the inner and outer boundary closely match the original MGFLD simulations, in Figure 2a and 2b we plot a comparison of the density, entropy, electron fraction, and velocity profiles for the one-dimensional simulation, B, and the corresponding MGFLD simulation. These two simulations were initiated from the same model and then run independently thereafter (except, of course, that simulation B uses the neutrino and boundary data generated by the MGFLD run). The comparison is made at 71 ms after bounce. Modulo differences at the shock, the agreement between the two simulations is excellent. Differences are expected at the shock because the PPM Godunov-type scheme is better able to resolve it than second-order artificial viscosity methods.

In Figure 3a, we include three two-dimensional entropy slices spanning the first 20 ms of our simulation C, which is a “hydrodynamics only” model. The development of protoneutron star

convection in the innermost region below the neutrinospheres (34 – 52 km) is evident. In the absence of neutrino transport, the redistribution of entropy and electron fraction by convection stabilizes this region, and convection dies out by $t_{\text{pb}} = 28$ ms. The redistribution of the entropy and electron fraction profiles by convection is shown in Figure 3c, where we plot the angle-averaged entropy and electron fraction versus radius at the same three time slices shown in Figure 3a. These quantities are defined as follows

$$\langle S \rangle (i) = \frac{1}{A(i)} \sum_{j=1}^{n_\theta} A(i, j) S(i, j) \quad (11)$$

and

$$\langle Y_e \rangle (i) = \frac{1}{A(i)} \sum_{j=1}^{n_\theta} A(i, j) Y_e(i, j) \quad (12)$$

where

$$A(i, j) = 2\pi r^2(i) \sin \theta(j) d\theta \quad (13)$$

and where $A(i) = 4\pi r^2(i)$ and $d\theta = \pi/128$. In equations (11) and (12), $S(i, j)$ and $Y_e(i, j)$ are our two-dimensional entropy and electron fraction configurations; the index i runs over $n_r = 128$ radial zones, and the index j runs over $n_\theta = 128$ angles. As $\theta \rightarrow 0$, the area of the strip on the 2-sphere spanned by $d\theta$, $A(i, j)$, approaches zero. The angle averaging in equations (11) and (12) is therefore designed to ensure that the averaged quantities near the poles contribute less. In Figure 3c, it is seen that at $t_{\text{pb}} = 13$ ms both entropy and electron fraction gradients are negative below 40 km, but by $t_{\text{pb}} = 18$ ms, the entropy gradient has become positive and is thus tending to stabilize the still negative gradient in electron fraction.

The additional entropy gradients in Figure 3c (*e.g.*, at 100 km) that appear below the shock with time result from the successive strengthening and weakening of the shock as it first propagates out after bounce and as the inner core oscillates in quasihydrostatic equilibrium. These gradients give rise to additional Ledoux unstable regions, and convection develops in these regions, seeded by the initial convection episode. This is evident in Figure 3a, at $t_{\text{pb}} = 28$ ms. The shock is clearly outlined by the large jump in entropy across it. The distortions in the shock’s sphericity when proton-neutron star convection reaches it are also evident.

In Figure 3b, we plot the angle-averaged radial and angular convection velocities, defined by

$$\langle v_c \rangle_r = \frac{1}{A(i)} \sum_{j=1}^{n_\theta} A(i, j) |v_r(i, j)| - \langle v \rangle \quad (14)$$

and

$$\langle v_c \rangle_\theta = \frac{1}{A(i)} \sum_{j=1}^{n_\theta} A(i, j) |v_\theta(i, j)| \quad (15)$$

where

$$\langle v \rangle = \frac{1}{A(i)} \sum_{j=1}^{n_\theta} A(i, j) |v_r(i, j)| \quad (16)$$

Within 10 ms, the radial convection velocity in the innermost region peaks between 3.7 and 5.0×10^8 cm/sec, whereas the angular convection velocity peaks at a somewhat larger value of 6.2×10^8 cm/sec. The radial convection velocity below the shock reaches a peak value of 10^9 cm/sec after about 20 ms; by then, the angular convection velocity has decreased. Note the anticorrelation between the radial and angular convection velocities. The peaks in the radial velocity correspond to troughs in the angular velocity and vice versa, which is characteristic of convective “rollover.”

In Figure 4a, we include three entropy slices spanning 21 ms in our simulation D. With the inclusion of neutrino transport, there is no evidence of protoneutron star convection. Providing more quantitative detail, Figure 4b shows that the angle-averaged radial and angular convection velocities peak at values orders of magnitude smaller than in simulation C. In the next section, we will present a simple analytical model that illustrates why this occurs.

Very important to the analysis we will present here and in the next section, and to the overall conclusions of this paper, is the angle-averaged radial fluid velocity (as opposed to the angle-averaged convection velocities). In Figure 4d, early in simulations D and L, we plot the fluid velocity as a function of radius with a focus on the innermost 100 km, where protoneutron star convection first develops in both simulations. Most important to note is that in simulation C, the convection velocities in this region are comparable to the fluid velocity; consequently, the convective transport of entropy and leptons is evident in Figure 3a. On the other hand, we see that the convection velocities in simulation D are orders of magnitude smaller than the fluid velocity, which explains why convective transport of entropy and leptons is not evident in Figure 4a.

In addition to the effect on the convection velocities, Figure 4c demonstrates transport’s effect on the innermost entropy gradient in the initial Ledoux unstable region. In this case, the entropy gradient is smoothed out by neutrino diffusion [see also Burrows *et al.* (1995)], whereas in simulation C, it was smoothed out by convection. Moreover, Figure 4c shows that the initial lepton gradient is more or less maintained by the same neutrino diffusion. More important, despite the maintenance of this gradient, we see no evidence of protoneutron star convection over the entire 100 ms spanned by our simulation, counter to what was seen by Burrows (1987), Burrows and Fryxell (1993), Burrows *et al.* (1995), and by Janka and Müller (1993b, 1994, 1995).

In a self-consistent multidimensional simulation with both multidimensional neutrino transport and hydrodynamics, matter irregularities would give rise to irregularities in the neutrino radiation fields. These would be smoothed out by neutrino transport, which in turn, coming full circle, would smooth out the original matter irregularities. The irregularities in the radiation fields would be smoothed out on transport time scales, which we neglect by imposing already spherically

symmetric neutrino distributions. To correct for this, in simulation E we take into account the time it takes for entropy and lepton transport to occur between a convecting fluid element and its surroundings, by modifying the entropy and lepton equilibration rates. This is done as outlined in the previous section. Of course, in a fully self-consistent simulation, the smoothed radiation field may ultimately be different than the spherically symmetric fields we impose. This is a shortcoming of our approximation that we cannot correct. However, we find that transport suppresses protoneutron star convection significantly, and in so doing, tends to keep the matter spherically symmetric, which in turn would keep the radiation fields close to our imposed fields.

Figure 5a includes three entropy slices spanning 20 ms in simulation E. Again, as in simulation D, where “finite-time” effects were not considered, there is no evidence of protoneutron star convection. More quantitatively, Figure 5b illustrates that the peak angle-averaged radial and angular convection velocities are almost an order of magnitude larger than they are in simulation D, but still roughly two orders of magnitude smaller than they are in simulation C (a “hydrodynamics only” model). Therefore, our conclusion that neutrino transport renders protoneutron star convection insignificant is not changed. Figure 5c shows once again the smoothing of the innermost entropy gradient and the maintenance of the lepton gradient by neutrino diffusion during the course of the simulation.

To further enhance protoneutron star convection’s chances of developing in the presence of neutrino transport, and to further explore the interplay between neutrino transport and protoneutron star convection, we have carried out several runs with “low-test” initial conditions, in which the initial entropy gradient, which initially drives protoneutron star convection, is maximized. Figure 6a includes three entropy slices from simulation F, in which neutrino transport is turned off. The large initial entropy gradient is evident in the first slice, and protoneutron star convection develops rather dramatically within 10 ms after the start of our run. After an additional 10 ms (at $t_{\text{pb}} = 27$ ms), convection has reached the shock and has distorted it significantly. Figure 6b shows the peak angle-averaged radial and angular convection velocities. At $t_{\text{pb}} \sim 16$ ms, the peak convection velocities for simulations C and F are comparable, but by

$t_{\text{pb}} \sim 26$ ms, the velocities in the innermost region in simulation F are roughly two times larger, and the outer peak in radial convection velocity is still developing, indicating that the convection growth time for simulation F is longer. Figure 6c shows the rather dramatic and rapid smoothing of the initial entropy and lepton fraction gradients below ~ 100 km that occurs in this simulation.

In Figure 7a, the three entropy slices show minimal protoneutron star convection developing within 10 ms of the start of simulation G, which includes neutrino transport, but begins with the same “low-test” initial conditions used in simulation F. However, by $t_{\text{pb}} = 27$ ms, at least in the two-dimensional entropy plot, the configuration appears once again to be spherically symmetric. Examination of the convection velocities in Figure 7b shows that, relative to simulation F, the velocities are reduced, particularly at $t_{\text{pb}} = 27$ ms, where they are significantly reduced. Figure 7c shows the smoothing of the entropy gradient in the initial Ledoux unstable region and the maintenance of the lepton gradient that is consistently exhibited by all of our two-dimensional simulations that include neutrino transport (simulations D,E,G, and H).

To help protoneutron star convection even more, we carried out simulation H, which uses the “low-test” initial conditions used in simulations F and G, and the reduced entropy and lepton equilibration rates used in simulation E. Figure 8a shows three entropy slices from this simulation. Again, at $t_{\text{pb}} = 17$ ms, minimal protoneutron star convection is evident, but after an additional 10 ms, the two-dimensional entropy configuration appears to be spherically symmetric. A look at Figure 8b shows that the peak radial and angular convection velocities are 5–10 times smaller relative to their values in simulation F (“low-test” initial conditions; “hydrodynamics only” model). Figure 8c shows the evolution in the entropy and electron fraction gradients, with the expected smoothing of the initial entropy gradient during the first 20 ms by neutrino diffusion, and the maintenance of the lepton gradient.

Figure 9 illustrates the long-term behavior in entropy in simulations D, E, and G. No convection is evident in simulation D at 86 ms into our run, and minimal convection is evident in simulation E at about the same time. In contrast, in the “low-test” simulation, G, more vigorous protoneutron star convection has developed at this later time in our run than appeared at earlier

times (see Figure 7a).

Figures 10a–c and 11a–c depict the evolution in entropy, convection velocities, and entropy and electron fraction gradients for our $15 M_{\odot}$ model. The same behavior exhibited by the $25 M_{\odot}$ model is exhibited here, indicating that our conclusions regarding neutrino transport’s tendency to inhibit the development of protoneutron star convection are independent of stellar mass and the size and profile of the initial precollapse or postbounce cores.

4. Analytical Model

Convection near or below the neutrinospheres can be profoundly influenced by the neutrino transport of energy and leptons between a convecting fluid element and the background. In effect, convection becomes “leaky,” and differences between a convecting fluid element’s entropy and lepton fraction and the background’s entropy and lepton fraction, from which the buoyancy force driving convection arises, are reduced. To construct the simplest model of this, we will assume that the lepton fraction gradient is zero and that convection is driven by a negative entropy gradient that is constant in space and time. [Reversing the roles of the entropy and lepton fraction gradients would give analogous results. The more general case in which both gradients are nonzero has been considered by Bruenn and Dineva (1996). This complicates the analysis and can lead to additional modes of instability, such as semiconvection and neutron fingers, which are not relevant here.] We will also assume that the effect of neutrino transport is to equilibrate the entropy of a fluid element with the background entropy in a characteristic time scale τ_s .⁷ If the fluid element and the background are in pressure balance, and if we neglect viscosity (microscopic and turbulent) and keep only first order terms, the fluid element’s equations of motion are

$$\dot{v} = \frac{g}{\rho} \alpha_s \theta_s \tag{17}$$

⁷We realize that temperature is the appropriate thermodynamic variable to describe the equilibration in energy of two systems in thermal contact, as is the chemical potential for equilibration in particle number. Because our system is in nuclear statistical equilibrium, it is legitimate to consider equilibration in terms of the variables s and Y_ℓ ; *i.e.*, when the temperatures and chemical potentials of the two systems in pressure balance become equal, their s ’s and Y_ℓ ’s are also equal. Using the same variables to describe equilibration that are used to describe convective instability greatly simplifies the picture.

$$\dot{\theta}_s = -\frac{\theta_s}{\tau_s} - \frac{d\bar{s}}{dr}v \quad (18)$$

where $\theta_s = s - \bar{s}$, with s and \bar{s} being the fluid element's entropy and the background's entropy, respectively; g is the local acceleration of gravity; v is the radial velocity; and $\alpha_s \equiv -(\partial\rho/\partial s)_{P,Y_\ell} > 0$, where Y_ℓ is the common lepton fraction. Equation (17) equates the fluid element's acceleration to the buoyancy force arising from the difference between its entropy and the background's entropy; equation (18) equates $\dot{\theta}_s$ to \dot{s} minus $\dot{\bar{s}}$, where \dot{s} results from the fluid element's equilibration with the background, and $\dot{\bar{s}}$ results from its motion through the gradient in \bar{s} .

If we neglect neutrino effects ($\tau_s = \infty$), the solutions to equations (17) and (18) indicate that (a) if $d\bar{s}/dr > 0$, the fluid element oscillates with the Brunt-Väisälä frequency $\omega_{BV_s} \equiv [(g\alpha_s d\bar{s}/dr)/\rho]^{1/2}$, and (b) if $d\bar{s}/dr < 0$, it convects, i.e., its velocity increases exponentially, and the convection growth time scale is given by $\tau = \tau_{BV_s} \equiv [-(g\alpha_s d\bar{s}/dr)/\rho]^{-1/2}$. When neutrino transport effects are included in the convectively unstable case ($d\bar{s}/dr < 0$), the fluid element convects, but the convection growth time scale $\tau > \tau_{BV_s}$ is given by $1/\tau = [1/\tau_{BV_s}^2 + 1/4\tau_s^2]^{1/2} - 1/2\tau_s$. In the limit $\tau_s \ll \tau_{BV_s}$, the growth time scale increases by τ_{BV_s}/τ_s , i.e., $\tau \simeq \tau_{BV_s}^2/\tau_s$.

In addition to reducing convection's growth rate, neutrino transport also reduces its asymptotic velocities. In particular, in the limit $\tau_s \ll \tau_{BV_s}$, the solutions to equations (17) and (18) show that a fluid element's velocity after moving a distance ℓ from rest is reduced by the factor τ_s/τ_{BV_s} .

To apply this analysis to protoneutron star convection, we note that $\tau_{BV_s} = 1.8$ ms at the neutrinosphere ($\rho \sim 3 \times 10^{11}$ g/cm³) and 1.4 ms at 10^{12} g/cm³. These values are representative of both models, S15s7b and S25s7b, after bounce, and are computed for a typical postbounce s gradient of 1, in 30 km, and no gradient in Y_ℓ . Similarly, $\tau_{BV_{Y_\ell}} = 12.3$ ms at the neutrinosphere

and 16.6 ms at 10^{12} g/cm³. These values are computed for a postbounce gradient of 0.1, in 30 km, and no gradient in s . On the other hand, our $\dot{\epsilon}$ from neutrino heating and cooling, including “finite-time” corrections, gives values for τ_s that decrease from 0.62 ms at the neutrinosphere to 0.03 ms at 10^{12} g cm⁻³, for our 25 M_⊙ model, and from 0.65 ms at the neutrinosphere to 0.028 ms at 10^{12} g cm⁻³, for our 15 M_⊙ model. Note that the numbers are fairly independent of the precollapse model. Our \dot{Y}_e , with “finite-time” corrections, gives lepton equilibration times of 0.049 ms at the neutrinosphere and 0.018 ms at 10^{12} g cm⁻³, for our 25 M_⊙ model, and 0.054 ms at the neutrinosphere and 0.017 ms at 10^{12} g cm⁻³, for our 15 M_⊙ model. These imply that neutrino transport should reduce the growth rate and asymptotic velocities of entropy-driven (lepton-driven) convection by a factor ~ 3 (50) at the neutrinosphere and a factor ~ 250 (1000) at 10^{12} g cm⁻³, for both the 15 and 25 M_⊙ models. Our simulations are consistent with these results.

5. Summary, Discussion, and Conclusions

In the absence of neutrino transport, for both our 15 and 25 M_{\odot} models the angle-averaged radial and angular convection velocities in the initial Ledoux unstable region below the shock after bounce achieve their peak values in ~ 20 ms, after which they decrease as the convection in this region dissipates. The dissipation occurs as the initial postbounce entropy and lepton gradients are smoothed out by convection. The initial protoneutron star convection episode seeds additional protoneutron star convection beneath the shock, which is driven by successive entropy gradients that develop above the initially unstable region, as the shock propagates out after core bounce and is in turn strengthened and weakened by the oscillating inner core.

In the presence of neutrino transport, protoneutron star convection velocities are too small relative to the bulk inflow velocities to result in any significant convective transport of entropy and leptons. Our two-dimensional entropy profiles remain for all intents and purposes spherically symmetric, and the peak angle-averaged radial and angular convection velocities are orders of magnitude smaller than they are in the corresponding “hydrodynamics only” models.

When neutrino transport is included in any of our simulations, the initial postbounce entropy gradient is smoothed out by neutrino diffusion, whereas the initial lepton gradient is maintained by electron capture and neutrino escape near the neutrinosphere. Counter to what was seen by Burrows (1987), Burrows and Fryxell (1993), Burrows *et al.* (1995), and by Janka and Müller (1993b, 1994, 1995), despite the persistence of the lepton gradient, protoneutron star convection develops in the 100 ms spanned by our simulations only in our “low-test” simulation, which begins with unrealistic initial entropy and lepton gradients that result from an unrealistic core collapse simulation with oversimplified neutrino transport.

We have included simulations in which the entropy and lepton equilibration rates (as defined in Section 2) were reduced by considering the neutrino diffusion time across a convecting element of pressure-scale-height size; i.e., by using the largest convecting element, we overestimate the equilibration suppression. Details can be found in Section 2. Despite the reduction in rates, our

conclusions are not altered. The two-dimensional entropy profiles show minimal protoneutron star convection development, and the ratio of the angle-averaged radial and angular convection velocities to their counterparts in the “hydrodynamics only” models remain small.

In other simulations, we optimized protoneutron star convection’s chances of developing by starting with “low-test” initial conditions. These conditions were generated by core collapse simulations that incorporated “low-test” neutrino transport, ignoring the important deleptonization effects of neutrino–electron scattering (NES), and the further deleptonization accompanying ion–ion screening corrections to the neutral-current coherent isoenergetic scattering on nuclei, which dominates the neutrino opacity during infall. It is well known that less deleptonization occurs when NES is neglected, resulting in a larger inner core, a stronger initial shock, a larger initial shock radius, and a larger initial entropy gradient that will subsequently drive a more vigorous protoneutron star convection. Whereas the initial protoneutron star convection episode in the “hydrodynamics only” model was rather dramatic, with neutrino transport included, the behavior observed in simulations beginning with realistic initial conditions was repeated: The two-dimensional entropy profiles showed very little protoneutron star convection, and the angle-averaged radial and angular convection velocities were significantly reduced relative to their values in the “hydrodynamics only” model. This occurred even in a final simulation in which we provided protoneutron star convection with its best chance of developing, by starting with “low-test” initial conditions while simultaneously implementing reduced entropy and lepton equilibration rates to account for neutrino diffusion.

A simple analytical model supports our numerical results, and demonstrates that neutrino transport reduces the convection growth rates and asymptotic velocities by a factor of τ_{BV_s}/τ_s , for entropy-driven convection, and by a factor of $\tau_{BV_{s,Y_\ell}}/\tau_{Y_\ell}$, for lepton-driven convection, where τ_s and τ_{Y_ℓ} are the time scales for equilibrating via neutrino transport a convecting element with the background, in entropy and leptons, respectively, and $\tau_{BV_{s,Y_\ell}}$ are the e-folding times for convection’s growth in the absence of neutrino transport. With “finite-time” corrections to the equilibration rates, the ratio τ_{BV_s}/τ_s ranges from ~ 3 –50 between the neutrinosphere and 10^{12}

gcm^{-3} ; the ratio $\tau_{BV_{Y_\ell}}/\tau_{Y_\ell}$ ranges from ~ 250 – 1000 .

Most prior multidimensional simulations of protoneutron star convection (*e.g.*, Burrows and Fryxell 1992, 1993, and Janka and Müller 1993b, 1996) have either ignored neutrino transport entirely, or have employed radial-ray neutrino transport. While the latter is necessitated by the extreme computational challenge imposed by true multidimensional transport, it ignores the tendency of neutrino transport to equilibrate upflows and downflows with each other in energy and leptons, thus reducing the very buoyancy contrast driving these flows. Our 1-D neutrino transport is complementary to radial-ray transport in this regard. Imposing a spherically symmetric neutrino distribution is equivalent to maximizing the lateral angular transport of neutrinos between ascending high-entropy and descending low-entropy convecting elements, which would be expected to suppress protoneutron star convection as the rising and falling flows equilibrate in entropy and leptons. No doubt differences between our results and those of the aforementioned groups derive in part from these two very different transport approximations (as well as from our use of multigroup transport and their use of gray transport, which in semitransparent regions breaks down).

To assess the validity of our neutrino transport approximation, *i.e.*, our use of a precalculated spherically symmetric neutrino distribution, we can compare our equilibration times with those obtained from detailed neutrino equilibration experiments (Bruenn *et al.* 1995, Bruenn & Dineva 1996, 1997). These are shown in Figure 12. The equilibration time scales τ_s and τ_{Y_ℓ} correspond to a perturbation of a fluid element in entropy and lepton fraction, respectively, and both equilibration time scales are computed for a fluid perturbation scale equal to 1 pressure scale height, which is ~ 10 km at all densities. For smaller length scales, the equilibration time scales would be reduced. As defined in Section 4, the Brunt-Väisälä time scale, τ_{BV_s} , is computed for a gradient in s of 1, in 30 km, and no gradient in Y_ℓ , and is appropriate for entropy-driven convection. Similarly, the Brunt-Väisälä time scale, $\tau_{BV_{Y_\ell}}$, is computed for a gradient in Y_ℓ of 0.1, in 30 km, and no gradient in s , and is appropriate for lepton-driven convection. Both τ_s and τ_{Y_ℓ} exhibit a minimum near the neutrinosphere. At higher densities they increase because of slow neutrino diffusion, and at low

densities they increase because of weak neutrino coupling with the matter.

The equilibration experiments show that a fluid element of one pressure scale height in radius will equilibrate in entropy in a minimum time of 3.1 ms, which occurs at $\sim 10^{11}$ g cm $^{-3}$. Smaller modes will equilibrate faster. The lepton equilibration time has a minimum of 0.29 ms, which also occurs at $\sim 10^{11}$ g cm $^{-3}$. On the other hand, our $\dot{\epsilon}$ (with “finite-time” corrections) gives τ_s values for our 25 M_\odot model that decrease from 0.62 ms at the neutrinosphere ($\sim 3 \times 10^{11}$ g cm $^{-3}$), which is ~ 10 times shorter than is observed in the equilibration experiments, to 0.03 ms at 10^{12} g cm $^{-3}$, which is ~ 333 times shorter than is observed in the equilibration experiments. Similarly, values for our 15 M_\odot model decrease from 0.65 ms at the neutrinosphere to 0.028 ms at 10^{12} g cm $^{-3}$. Our \dot{Y}_e (with “finite-time” corrections) gives τ_{Y_e} values for our 25 M_\odot model that decrease from 0.049 ms at the neutrinosphere, which is ~ 6 times shorter than is observed in the equilibration experiments, to 0.018 ms at 10^{12} g cm $^{-3}$, which is ~ 38 times shorter than is observed in the equilibration experiments. Similarly, values for our 15 M_\odot model decrease from 0.054 ms at the neutrinosphere to 0.017 ms at 10^{12} g cm $^{-3}$.

Because the density in the initial Ledoux unstable region in our 25 M_\odot model ranges from 6.9×10^{11} g/cm 3 at the top of the region to 1.38×10^{12} g/cm 3 at the bottom, and in our 15 M_\odot model ranges from 5.49×10^{11} g/cm 3 to 1.52×10^{12} g/cm 3 , at the outset of our simulations we are in a density range in which, based on our time scale analysis, we may seriously overestimate the entropy and lepton equilibration rates, even with “finite-time” corrections. Whether or not we must revise our conclusions regarding the effect of neutrino transport on the growth of convection depend, as we discuss below, on the type of protoneutron star convection.

- *Entropy-Driven or Entropy- and Lepton-Driven Convection:* As shown in Figure 12, the ratio of the Brunt-Väisälä time scales to the entropy equilibration time scales given by the equilibration experiments is always greater than unity, implying that the equilibration time is longer than the convection growth time. Therefore, based on this alone, there is no doubt that in our approximation we overestimate transport’s effect in suppressing convection.

- *Lepton-Driven Convection:* On the other hand, after the unstable entropy gradients have been eliminated by an initial round of entropy-driven convection, or by neutrino diffusion, protoneutron star convection tends to continue, driven by a negative lepton fraction gradient maintained by ongoing deleptonization at the neutrinosphere. This lepton-driven protoneutron star convection is forced by lepton fraction differences between convecting fluid elements and the background. For this case, the appropriate lepton equilibration time scales are given in Figure 12 by τ_{Y_ℓ} . Figure 12 also shows the appropriate Brunt-Väisälä time scales, $\tau_{BV_{Y_\ell}}$. The lepton equilibration time scales are significantly smaller than the convection growth times ($\tau_{BV_{Y_\ell}}$) for densities between 3×10^{10} and 3×10^{12} g cm⁻³; therefore, in the case of lepton-driven convection, which is the most important of protoneutron star convection modes, our conclusions regarding the tendency of neutrino transport to severely suppress convection are realistic.

To conclude: There is clearly a need to self-consistently couple multidimensional multigroup realistic neutrino transport and multidimensional hydrodynamics in optically thick regions before we or any other group can draw final conclusions regarding the development of protoneutron star convection, or any mode of convection below the neutrinospheres, in core collapse supernovae. Nonetheless, our compendium of results, supported by our analytical model and time scale analyses, is compelling, pointing to a very real effect: Neutrino transport will suppress protoneutron star convection, the extent of which lies somewhere between what we have computed and what other groups have computed. The question is: Where?

6. Acknowledgements

AM, ACC, MWG, and MRS were supported at the Oak Ridge National Laboratory, which is managed by Lockheed Martin Energy Research Corporation under DOE contract DE-AC05-96OR22464. AM, MWG, and MRS were supported at the University of Tennessee under DOE contract DE-FG05-93ER40770. ACC and SU were supported at Vanderbilt University under DOE contract DE-FG02-96ER40975. SWB was supported at Florida Atlantic University under NSF grant AST-9618423 and NASA grant NRA-96-04-GSFC-073, and JMB was supported at North Carolina State University under NASA grant NAG5-2844.

The simulations presented in this paper were carried out on the Cray C90 at the National Energy Research Supercomputer Center, the Cray Y/MP at the North Carolina Supercomputer Center, and the Cray Y/MP and Silicon Graphics Power Challenge at the Florida Supercomputer Center.

We would like to thank Thomas Janka for stimulating discussions, and the referee, Marc Herant, for many useful criticisms and suggestions that considerably expanded and strengthened the content of this work.

7. References

- Arnett, W. D. 1986, in IAU Symposium 125, The Origin and Evolution of Neutron Stars, ed. D. J. Helfand and J. H. Huang (Dordrecht: Reidel)
- Arnett, W. D. 1987, *ApJ*, 319, 136
- Bazan, G. & Arnett, W. D. 1994, *ApJ*, 433, L41
- Bethe, H. A. 1990, *Rev. Mod. Phys.*, 62, 801
- Bethe, H. A. 1993, *ApJ*, 412, 192
- Bethe, H. A., Brown, G. E., & Cooperstein, J. 1987, *ApJ*, 322, 201
- Bethe, H. & Wilson, J. R. 1985, *ApJ*, 295, 14
- Bruenn, S. W. 1993, in *Nuclear Physics in the Universe*, eds. M. W. Guidry and M. R. Strayer (IOP Publishing, Bristol), p. 31
- Bruenn, S. W., Buchler, J. R., & Livio, M. 1979, *ApJ*, 234, L183
- Bruenn, S. W. & Dineva, T. 1996, *ApJ*, 458, L71
- Bruenn, S. W. & Dineva, T. 1997, in preparation
- Bruenn, S. W. & Mezzacappa, A. 1994, *ApJ*, 433, L45
- Bruenn, S. W., Mezzacappa, A., & Dineva, T. 1995, *Phys. Rep.*, 256, 69
- Burrows, A. 1987, *ApJ*, 318, L63
- Burrows, A. & Fryxell, B. A. 1992, *Science*, 258, 430
- Burrows, A. & Fryxell, B. A. 1993, *ApJ*, 418, L33
- Burrows, A., Hayes, J., & Fryxell, B. A. 1995, *ApJ*, 450, 830
- Burrows, A. & Lattimer, J. M. 1988, *Phys. Rep.*, 163, 5

- Colgate, S. A., Herant, M., & Benz, W. 1993, *Phys. Rep.*, 227, 157
- Colgate, S. A., & Petschek, A. G. 1980, *ApJ*, 236, L115
- Cooperstein, J. 1993, in *Nuclear Physics in the Universe*, eds. M. W. Guidry and M. R. Strayer (IOP Publishing, Bristol), p. 99
- Epstein, R. I. 1979, *MNRAS*, 188, 305
- Herant, M., Benz, W., & Colgate, S. A. 1992, *ApJ*, 395, 642
- Herant, M., Benz, W., Hix, W. R., Fryer, C. L., & Colgate, S. A. 1994, *ApJ*, 435, 339
- Janka, H.-Th. & Müller, E. 1993a, in *Proc. of the IAU Coll. 145 (Xian China, May 24–29, 1993)*, eds. R. McCray and Wang Zhenru, (Cambridge Univ. Press, Cambridge); MPA-Preprint 748
- Janka, H.-Th. & Müller, E. 1993b, in *Frontiers of Neutrino Astrophysics*, eds. Y. Suzuki and K. Nakamura, (Universal Academy Press, Tokyo). p. 203
- Janka, H.-Th. & Müller, E. 1995, *ApJ*, 448, L109
- Janka, H.-Th., & Müller, E. 1996, *A&A* 306, 167
- Keil, W., Janka, H.-Th, & Müller, E. 1996, *ApJ*, 473, L111
- Lattimer, J. M., & Mazurek, T. J. 1981, *ApJ*, 246, 995
- Lattimer, J. M. & Swesty, F. D. 1991, *Nucl. Phys. A*, 535, 331
- Livio, M., Buchler, J. R., & Colgate, S. A. 1980, *ApJ*, 238, L139
- Mayle, R. W. 1985, Ph.D. Thesis, Univ. California, Berkeley (UCRL preprint no. 53713)
- Mezzacappa, A. & Bruenn, S. W. 1993, *ApJ*, 405, 669
- Mezzacappa, A., Calder, A. C., Bruenn, S. W., Blondin, J. M., Guidry, M. W., Strayer, M. R., & Umar, A. S. 1997, *ApJ*, in press

- Miller, D. S., Wilson, J. R., & Mayle, R. W. 1993, *ApJ*, 415, 278
- Müller, E. 1993, in *Proc. of the 7th Workshop on Nuclear Astrophysics (Ringberg Castle, March 22–27, 1993)*, eds. W. Hillebrandt and E. Müller, Report MPA/P7, Max-Planck-Institut für Astrophysik, Garching, p. 27
- Müller, E. & Janka, H.-Th. 1994, in *Reviews in Modern Astronomy 7 (Proc. of the Int. Conf. of the AG (Bochum, Germany, 1993))*, eds. G. Klure (Astronomische Gesellschaft, Hamburg), p. 103
- Shimizu, T., Yamada, S., & Sato, K. 1993, *Publ. Astron. Soc. Japan*, 45, L53
- Shimizu, T., Yamada, S., & Sato, K. 1994, *ApJ*, 432, L119
- Smarr, L., Wilson, J. R., Barton, R. T., & Bowers, R. L. 1981 *ApJ*, 246, 515
- Weaver, T. A. & Woosley, S. E. 1997, *ApJ*, in preparation
- Wilson, J. R. 1985, in *Numerical Astrophysics*, eds. J. M. Centrella *et al.* (Boston: Jones & Bartlett), 422
- Wilson, J. R. & Mayle, R. W. 1988, *Phys. Rep.*, 163, 63
- Wilson, J. R. & Mayle, R. W. 1993, *Phys. Rep.*, 227, 97
- Wilson, J. R., Mayle, R. W., Woosley, S. E., & Weaver, T. 1986, *Ann. N.Y. Acad. Sci.*, 470, 367
- Woosley, S. E. & Weaver, T. A. 1995, *ApJS*, 101, 181

Simulation	Initial Time	Postbounce Time	Description
	(ms)	(ms)	
25 M_⊙ Models			
A	297.9	8.3	1-d hydro only
B	297.9	8.3	1-d hydro + ν transport
C	297.9	8.3	2-d hydro only
D	297.9	8.3	2-d hydro + ν transport
E	297.9	8.3	2-d “Finite Time” hydro + ν
F	299.4	7.23	2-d “Low Test” hydro only
G	299.4	7.23	2-d “Low Test” hydro + ν
H	299.4	7.23	2-d “F. T. L. T.” hydro + ν
15 M_⊙ Models			
I	211.1	11.9	1-d hydro only
J	211.1	11.9	1-d hydro + ν transport
K	211.1	11.9	2-d hydro only
L	211.1	11.9	2-d hydro + ν transport

Table 1: Simulation “start times” and descriptions.

Simulation	Seeding Radii		Entropy		Electron Fraction	
	(km)		(s = S/kN _B)		(Y _e) _{min}	(Y _e) _{max}
	r_{\min}	r_{\max}	s_{\min}	s_{\max}		
25 M_⊙ Models						
A	33.8	52.0	5.08	6.24	0.118	0.221
B	33.8	52.0	5.08	6.24	0.118	0.221
C	33.8	52.0	5.08	6.24	0.118	0.221
D	33.8	52.0	5.08	6.24	0.118	0.221
E	33.8	52.0	5.08	6.24	0.118	0.221
F	55.4	122.2	3.33	7.74	0.213	0.463
G	55.4	122.2	3.33	7.74	0.213	0.463
H	55.4	122.2	3.33	7.74	0.213	0.463
15 M_⊙ Models						
I	31.0	54.2	5.25	6.19	0.116	0.234
J	31.0	54.2	5.25	6.19	0.116	0.234
K	31.0	54.2	5.25	6.19	0.116	0.234
L	31.0	54.2	5.25	6.19	0.116	0.234

Table 2: Radial ranges, and entropy and electron fraction maxima and minima, for the initial Ledoux unstable regions.